JGR Atmospheres

RESEARCH ARTICLE
10.1029/2025JD045497

Double Low-Level Jets Over South China in the Warm Season: Diversity and Impacts

Chunling Zhou[1], Guixing Chen[1], Yu Du[1], and Lin Su[1]

[1]School of Atmospheric Sciences, Guangdong Province Key Laboratory for Climate Change and Natural Disaster Studies, Key Laboratory of Tropical Atmospheric-Ocean System (Ministry of Education), Sun Yat-sen University, and Southern Marine Science and Engineering Guangdong Laboratory (Zhuhai), Zhuhai, China

Key Points:

- Three types of double low-level jets (DLLJs) are distinguished by wind structures related to the positioning of synoptic disturbances
- Nocturnal wind maxima of DLLJs are driven by enhanced pressure gradient force due to pressure tides and weakened friction
- DLLJs induce low-level lifting that depends on wind structures and local terrains, producing robust differences in rainfall patterns

Supporting Information:

Supporting Information may be found in the online version of this article.

Correspondence to:

G. Chen and Y. Du,
chenguixing@mail.sysu.edu.cn;
duyu7@mail.sysu.edu.cn

Citation:

Zhou, C., Chen, G., Du, Y., & Su, L. (2026). Double low-level jets over South China in the warm season: Diversity and impacts. *Journal of Geophysical Research: Atmospheres*, *131*, e2025JD045497. https://doi.org/10.1029/2025JD045497

Received 24 SEP 2025
Accepted 18 MAR 2026

Abstract In South China, boundary layer jets (BLJs) often coexist with synoptic-system-related low-level jets (SLLJs) aloft, forming double low-level jets (DLLJs). This study examines the structural diversity of DLLJs and their impacts on rainfall. DLLJs are classified by their horizontal positioning into three types: Type-C (Connected, comprising 66% of all DLLJ events) with partial overlap, Type-O (Overlapped, 31%) with nearly coincident cores, and Type-D (Displaced, 3%) without overlap. Type-C develops mainly between continental low pressure and South China Sea high-pressure systems during April–June. Type-O occurs primarily south of land-based low-pressure anomalies during June–August, and Type-D is frequent during April–May along high-pressure flanks. All BLJs and SLLJs exhibit nocturnal wind maxima, primarily caused by the combined effects of enhanced pressure gradient force from pressure tides and weakened friction. In Type-O, SLLJs display an afternoon increase in wind speed, as weak oceanic friction at 750 hPa cannot offset daytime acceleration from pressure tides. DLLJs strongly modulate rainfall patterns through low-level lifting that depends on wind structures and local terrains. Type-C generates two rainbands: one on the windward side of Nanling Mountains, driven by the orographic lifting and BLJ-SLLJ coupling, and another over the Yangtze River Basin, associated with SLLJ hydraulic jumps on the leeside of Nanling Mountains and low-level shear convergence. Type-O enhances coastal rainfall by deep-layer convergence from overlapping BLJs and SLLJs combined with coastal orographic lifting. Type-D yields the weakest rainfall related to weaker BLJs. These results highlight the structural diversity of DLLJs and provide new insights for improving rainfall forecasts.

Plain Language Summary In South China, two different strong wind streams often form in the lower atmosphere: boundary layer jets and synoptic-system-related low-level jets. When they occur together, they create double low-level jets (DLLJs). This study found that DLLJs can be grouped into three structural types that are closely associated with the seasonal variations in dominant synoptic disturbances. They can lead to different rainfall patterns, as a result of the low-level lifting induced by various wind structures and complex terrains. The findings improve our understanding of DLLJ diversity and may help promote rainfall forecasts.

1. Introduction

Low-level jets (LLJs), defined by wind speed maxima within the boundary layer or lower troposphere, are profound atmospheric phenomena (Lima et al., 2018; Rife et al., 2010; Stensrud, 1996). In East Asia, LLJs mainly occur during the active period of southwesterly monsoon flows and greatly regulate summer rainbands (Chen et al., 2006, 2017; He et al., 2016). Southwesterly LLJs can transport abundant moisture from tropical oceans to the continent, and enhance low-level lifting and convective instability at their northern terminus, thereby triggering heavy rainfall (Bonner, 1968; Chen et al., 2014; Higgins et al., 1997; Monaghan et al., 2010; Wang & Chen, 2025; Zeng at al., 2022). Thus, understanding LLJs' activities and impacts is vital for studying extreme weather and regional climate in East Asia and for improving weather forecasts.

LLJs exhibit considerable variability in vertical structures and spatial distribution. Based on the height of wind speed maxima, LLJs are classified into boundary layer jets (BLJs) below 1 km and synoptic-system-related LLJs (SLLJs) at 1–4 km (Chen et al., 1994; Du et al., 2014; Zheng et al., 2026). In South China (Figure 1a), both types of LLJs occur frequently (Dong et al., 2021; Du et al., 2022; Kong et al., 2020; Li & Du, 2021; Li et al., 2020; Lin & Du, 2025; Zhang et al., 2024). BLJs typically develop over adjacent oceans, such as the Beibu Gulf (BBG, also known as the Gulf of Tonkin) and the northern South China Sea (NSCS) (Figure 1b), whereas SLLJs tend to form on the land of South China in association with westerly disturbances (Figure 1c). When BLJs and SLLJs coexist, they form double LLJs (DLLJs; Du et al., 2012). Previous case studies of extreme events have revealed three

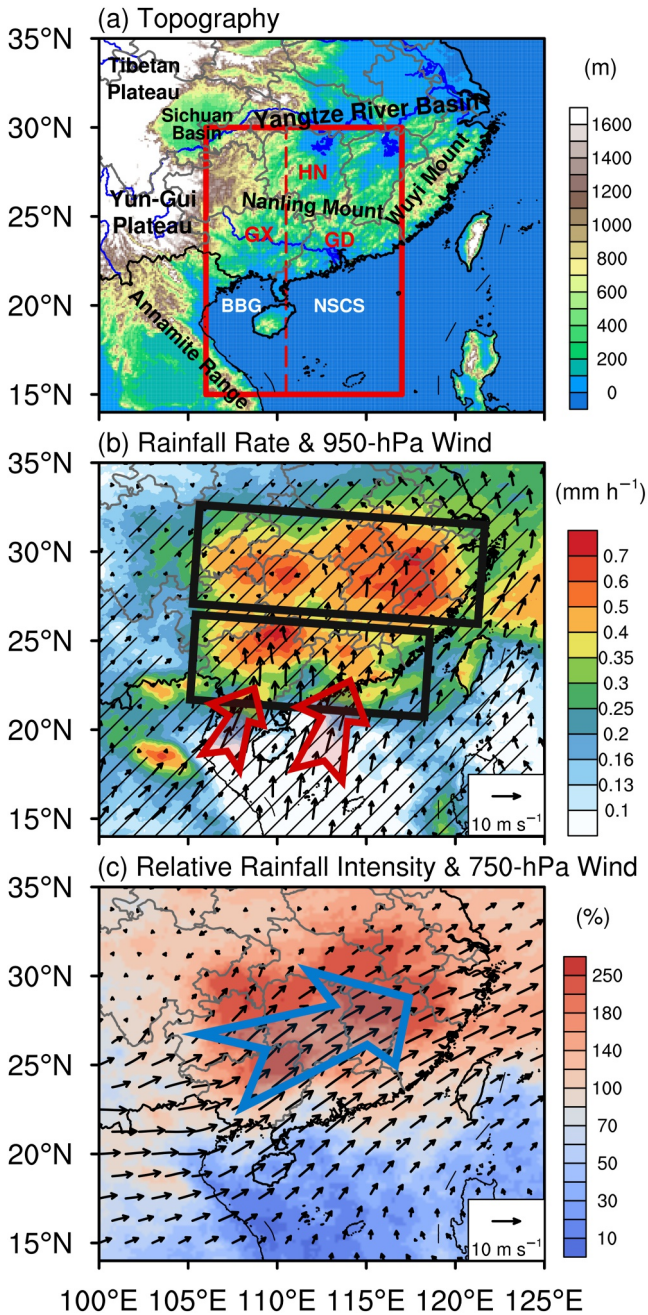

Figure 1. (a) The terrain height (shading, m) in South China. The red box is the region selected for double low-level jet (DLLJ) identification. The left (right) side of the red dashed line corresponds to the DLLJ subregions in the BBG (NSCS). Red labels represent Guangdong Province (GD), Guangxi Province (GX), and Hunan Province (HN). (b) Composite mean precipitation rates (shading, mm h^{-1}) and 950-hPa horizontal winds (vectors, m s^{-1}) during the identified DLLJ events over the BBG and the NSCS from April to September (2001–2023). The hatched areas denote statistical significance at the 95% confidence level. (c) Composite 750-hPa horizontal winds (vectors, m s^{-1}) and relative rainfall intensity (shading, %) for all DLLJ events. The relative rainfall intensity refers to the ratio of the mean precipitation rate during DLLJ events to the climatological mean precipitation rate. Blue and red arrows represent the wind cores of SLLJs and boundary layer jets, respectively, during all DLLJ events.

spatial configurations of DLLJs based on the relative positioning between BLJs and SLLJs: (a) coexisting with a certain horizontal distance (Du & Chen, 2019b), (b) partially overlapping, where land-based SLLJs extend over marine BLJs (Du & Chen, 2019b; Yang et al., 2025; Zhou et al., 2022), (c) nearly complete overlapping of the two jets (Luo & Du, 2023; Zhou et al., 2022). These configurations of BLJs and SLLJs indicate various wind structures, which are probably associated with the evolution of synoptic disturbances. Although these three DLLJ configurations have been identified in case studies, their climatological behavior remains less understood. A further investigation of DLLJs' diversity is thus crucial for our understanding of LLJ activities.

LLJs in South China often persist for several days and exhibit pronounced diurnal cycles, indicating modulation by both synoptic-scale disturbances and regional subdaily forcings. On the synoptic scale, LLJs often develop along the northwestern periphery of the Western Pacific Subtropical High or the southeastern flank of low-pressure systems, where enhanced pressure gradients favor their formation (He et al., 2016; Liu et al., 2023; Wang et al., 2003). On the subdaily time scale, LLJs typically peak between midnight and predawn (Du & Chen, 2019a; Du et al., 2014). Their nocturnal strengthening may arise from two key processes: (a) inertial oscillation in winds driven by the diurnally varying boundary-layer turbulent mixing (Blackadar, 1957; Xue et al., 2018), and (b) diurnally varying pressure gradients driven by horizontal thermal contrasts over sloped terrains (Holton, 1967) or between land and sea (Du, Rotunno et al., 2015; Du, Chen et al., 2015). Moreover, regional pressure gradients may be regulated by global pressure tides, particularly semi-diurnal cycles (Huang et al., 2010; Lindzen & Chapman, 1969). While these mechanisms are widely used to explain diurnal LLJ cycles, their combined effects under different synoptic backgrounds remain unclear, especially for the formation of LLJs at different altitudes and in different regions. Therefore, investigating the formation dynamics of various DLLJ types will enhance our understanding of the physical processes governing DLLJ diversity.

It is widely recognized that DLLJs play a key role in heavy rainfall by fostering favorable dynamic and thermodynamic environments (Cui et al., 2023; Du & Chen, 2018; Huang et al., 2022; Luo & Du, 2025; Liu et al., 2020; Ma et al., 2023; Zhang & Meng, 2019; Zhou et al., 2022). For instance, Du and Chen (2019b) noted that coupling between BLJs' exits and SLLJs' entrances produces boundary-layer convergence and mid-level divergence, thereby strengthening low-level lifting and convective initiation. Luo and Du (2023) revealed that the overlapping of BLJs and SLLJs can generate a deep convergence/lifting layer that may support long-lived convective systems. Xu et al. (2023) further showed that the coupling of 925-hPa BLJs and 850-hPa SLLJs enhances the poleward transport of moist static energy and increases vertical wind shear and vorticity, ultimately intensifying rainfall. Su et al. (2025) highlighted that the different BLJ-SLLJ configurations may modulate moisture fluxes, leading to different rainfall patterns in South China. In addition, LLJs at varying altitudes may interact with local terrain, where orographic lifting and coastal convergence further influence rainfall distribution (Du & Chen, 2019a; Du et al., 2020). Collectively, these previous studies based on extreme case analyses indicate that the impacts of DLLJs on rainfall strongly depend on their structural characteristics, including altitude, orientation, and interactions with terrain. This highlights the need for a climatological perspective to examine how different

DLLJ types modulate rainfall through their dynamic and thermodynamic processes, which is essential for clarifying the complex rainfall patterns in South China.

Previous studies have shown that DLLJs are active in South China and greatly regulate rainfall. This study conducts a climatological analysis of DLLJ diversity, focusing on their characteristics, formation processes, and rainfall impacts. We also pay attention to the regional contrasts between BBG and NSCS, because of some differences in terrains, background flows, and distances to westerly disturbances. Double low-level jets (DLLJs) are categorized into three types based on the relative distances between BLJs and SLLJs, allowing for comparison of their differences. The paper is organized as follows. Section 2 introduces data and methods. Section 3 presents the climatology of the three DLLJ types during the warm season, including their occurrence frequency, duration, spatial patterns, and temporal variations. Section 4 examines the synoptic disturbances and regional subdaily forcings that govern the formation of each type. Section 5 further discusses their detailed impacts on rainfall. Section 6 presents the relationship between the DLLJs in the BBG and the NSCS. Finally, Section 7 provides conclusions and discussions.

2. Data and Method

2.1. Data

To characterize the atmospheric conditions associated with DLLJs, we employ the fifth-generation atmospheric reanalysis from the European Centre for Medium-Range Weather Forecasts (ERA5; Hersbach et al., 2020). The ERA5 reanalysis provides a horizontal resolution of 0.25°, hourly temporal intervals, and 37 vertical pressure levels, which performs well in representing diurnal wind cycles over China (Chen et al., 2021). Note that, the 12-hr window of data assimilation in the ERA5 reanalysis induces artificial drops in wind speeds over South China around 1700–1800 and 0500–0600 Local Solar Time (LST) (Chen et al., 2021; Jourdier, 2020). To minimize this issue, we apply a five-point running average to the data for the diurnal cycle analysis (Section 4.2). Rainfall distributions related to DLLJs are examined using the latest version of Integrated Multi-satellite Retrievals for GPM, which offers a 30-min temporal interval and 0.1° spatial resolution (IMERG; Huffman et al., 2023). The IMERG data effectively capture the diurnal variations of rainfall, although the early morning rainfall intensity is slightly overestimated (Cui et al., 2020; Li et al., 2018). Both ERA5 and IMERG data sets were analyzed for the warm season (April–September) from 2001 to 2023. The results of this study rely on the reliability of ERA5 to represent LLJ structures and of IMERG to capture rainfall patterns. In addition, we identify the days with a tropical cyclone located west of 120°E and exclude such days from our analysis. The best-track data set of tropical cyclones is provided by the Shanghai Typhoon Institute (Ying et al., 2014).

2.2. Definition and Classification of Regional DLLJ Events

In this study, we mainly focus on the regional events of DLLJs. We examined two key sub-regions (Figure 1a): the BBG with its northern land (106°E–110.5°E, 15°N–30°N) and the NSCS with its northern land (110.5°E–117°E, 15°N–30°N). For brevity, these are hereafter referred to as DLLJs over the BBG and NSCS, respectively. The definition and classification of regional DLLJ events involve three steps: (a) identifying BLJ and SLLJ occurrences at given grid points; (b) defining regional events based on the horizontal extents of the LLJs; and (c) classifying DLLJ types by the distances between BLJs and SLLJs.

Step 1: Identification of LLJs at given grid points

Following a modified approach from Du and Chen (2019a), we define the criteria for identifying LLJs as follows: the maximum wind speed within the lowest 400-hPa layer above the surface must exceed 10 m s^{-1}, and the wind speed must decrease by at least 2.5 m s^{-1} from the height of the wind maximum to the wind minimum above it. A BLJ is identified when the level of maximum winds is within the lowest 100 hPa above the surface with a southerly wind. An SLLJ is identified when the maximum wind level is between the lowest 100 hPa and the lowest 400 hPa above the surface, with a southwesterly wind.

Step 2: Definition of the regional LLJ events based on horizontal extents

We focus on the regional events of LLJs that have a spatial scale of meso-α (Orlanski, 1975) or larger and last for several hours. First, we consider that the regional LLJs shall have a certain zonal extent. We adopt a criterion that the grid points meeting the criteria of Step 1 are more than a proportion (15%) at any given latitude in the sub-

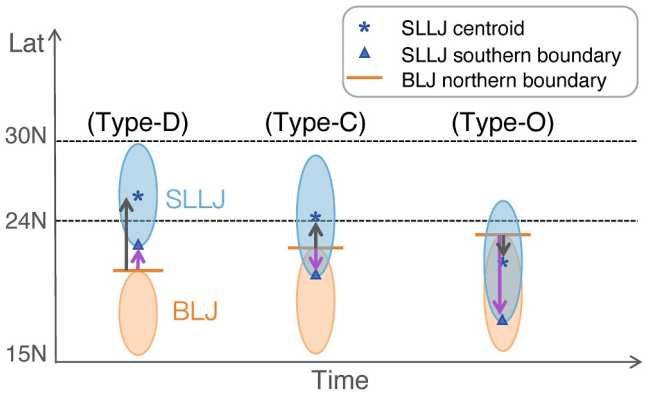

Figure 2. Schematic diagram illustrating the classification of double low-level jet types. Blue (orange) shadows indicate SLLJ (boundary layer jet (BLJ)) latitudinal extents. Black arrows depict the direction from the BLJ northern boundary toward the SLLJ centroid, while purple arrows represent the direction from the BLJ northern boundary toward the SLLJ southern boundary. Type-D, Type-C, and Type-O correspond to the displaced, connected, and overlapped configurations between BLJs and SLLJs, respectively.

regions. Second, we also require that the wind field be consistently strong in the regions of interest during the regional LLJ events. The wind speeds in the vicinity of LLJs are slightly smaller but comparable to those in the LLJs. Thus, we introduce an additional criterion that the zonal-mean wind speed in the sub-regions exceeds 10 m s^{-1} in the key layers of 950 and 750 hPa. These key layers have the maximum occurrences of BLJs and SLLJs, respectively (Du & Chen, 2019a).

We further examine the positions of regional LLJs. The BLJs are mostly observed near the coast of South China within 15°N–24°N, and they are always located south of SLLJs (Du & Chen, 2019a; Du et al., 2014). To estimate their relative distance, we identify the northern boundary of BLJs and the southern boundary of SLLJs. We also identify the centroid of SLLJs as the average of two latitudes: one with the highest proportion of grid points meeting the criteria of Step 1, and the other with the strongest zonal-mean wind speed at 750 hPa.

Step 3: Classification of DLLJ types.

Based on the relative distances between the BLJ's boundary and SLLJ's boundary/centroid, we can categorize DLLJs into three types as shown in the conceptual diagram in Figure 2:

- Type-D (Displaced): SLLJ's southern boundary is in the north of BLJ's northern boundary, with no overlapping edges.
- Type-C (Connected): SLLJ's southern boundary is in the south of the BLJ's northern boundary, but its centroid lies outside the BLJ domain (partial overlap).
- Type-O (Overlapped): The southern boundary and the centroid of the SLLJ lie within BLJ's domain, indicating core overlap.

Finally, a DLLJ event is defined when the same DLLJ type lasts for at least 3 hrs, allowing for an interruption of up to 1 hr. An example defining the three types of DLLJs in April 2001 and 2002 is shown in Figure S1 of Supporting Information S1.

3. Characteristics of the Three DLLJ Types

3.1. Occurrence Frequency and Duration

Figures 3a and 3b show the occurrence frequencies of the three DLLJ types. From April to September during 2001–2023, a total of 691 DLLJ events were identified over the BBG and 317 over the NSCS. Among them, 461 cases in the BBG and 204 cases in the NSCS are categorized as Type-C events, which feature partial overlap between BLJs and SLLJs, making this the most frequent category (accounting for 66% of all events). In addition, 308 Type-O events (30% of all events), marked by almost horizontal overlap of BLJs and SLLJs, are identified, including 220 in the BBG and 88 in the NSCS. Only a small fraction (4%) are classified as Type-D, where BLJs and SLLJs do not overlap. Notably, most DLLJs documented in previous studies (Du & Chen, 2019b; Zhou et al., 2022) fall into Type-C under this classification, highlighting their pivotal role in the initiation of convection.

Figures 3c and 3d illustrate the duration of the three DLLJ types. The mean durations of Type-C and Type-O events are 7–8 hr, with most cases lasting from 4 to 10 hr. In contrast, Type-D events are shorter lived, with a mean duration of 4–5 hr. In the BBG, Type-O events tend to persist slightly longer than Type-C events (Figure 3c), whereas in the NSCS, the mean duration of Type-O events is 1.15 hr shorter than that of Type-C events (Figure 3d). These multi-hour lifetimes suggest that DLLJs are governed by both synoptic-scale systems and regional subdaily forcings, an aspect further examined in the following analysis of physical processes.

3.2. Spatial Patterns of DLLJs

Figure 4 depicts the horizontal structures of the three DLLJ types. As expected, in the BBG, strong BLJs exceeding 10 m s^{-1} at 950 hPa are observed over the ocean for all DLLJ types (warm contours and vectors in Figures 4a–4c). Type-D shows the weakest BLJs and the smallest horizontal extent, dominated by southeasterly

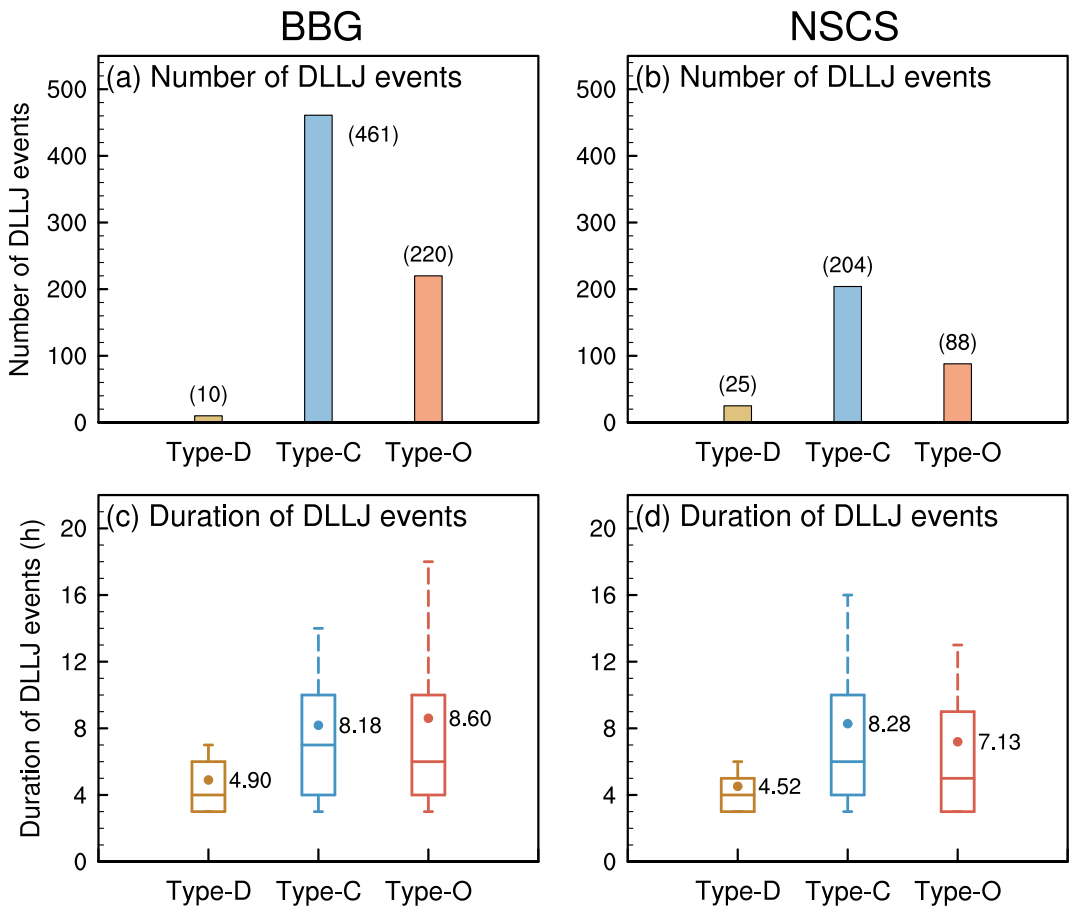

Figure 3. (a, b) Number (counts) of double low-level jet (DLLJ) events by type for (a) the BBG and (b) the NSCS. Values in parentheses indicate the total number of events. (c, d) Box-and-whisker plots showing the duration (hours) of each DLLJ type for (c) the BBG and (d) the NSCS. The middle point represents the mean duration of the DLLJ events, the line in the box indicates the median, the top and bottom of the box represent the interquartile range, and the upper (lower) short lines denote the 90th (10th) percentile.

winds (Figure 4a). BLJs in Type-C reach a maximum speed of 12 m s^{-1}, primarily from southerly flows (Figure 4b). Type-O displays the highest BLJ intensity, with peak winds of 14 m s^{-1} from southwesterly flows (Figure 4c). At 750 hPa, southwesterly winds associated with SLLJs are present in all types (cold contours and vectors in Figures 4a–4c). The SLLJ core in Type-D is located near 27°N, displaced from the marine BLJ (Figure 4a). Type-C features a broader area of SLLJ winds exceeding 10 m s^{-1} that extends farther south, partially overlapping with the BLJ (Figure 4b). In Type-O, moderate-intensity SLLJ shifts ocean-ward, coinciding with the BLJ and extending northeastward (Figure 4c). These features indicate that DLLJ types primarily depend on the position and extent of the SLLJs. The intensity of BLJs increases as the SLLJs approach the coast, suggesting that the southward propagation of synoptic disturbances may enhance the marine BLJs.

In the NSCS, BLJs in all three types are located over the ocean (warm contours and vectors in Figures 4d–4f). BLJs in Type-D are the weakest and dominated by southeasterly flows (Figure 4d), while BLJs in Type-C are characterized by southerly winds peaking at 12 m s^{-1} (Figure 4e). BLJs in Type-O are mainly southwesterly winds with the largest spatial extent (Figure 4f). SLLJs in all types also display southwesterly flows but differ notably in their north–south positioning (cold contours and vectors in Figures 4d–4f). In Type-D, SLLJs are situated north of 25°N and remain separated from the marine BLJs (Figure 4d), covering a larger area than those in the BBG (Figure 4a). Type-C exhibits the strongest SLLJs (Figure 4e), positioned farther southeast than those over the BBG (Figure 4b). SLLJs in Type-O are located over the NSCS, overlapping with the BLJs (Figure 4f). In addition, for the same DLLJ type, SLLJs in the NSCS show a more pronounced zonal wind component than those in the BBG.

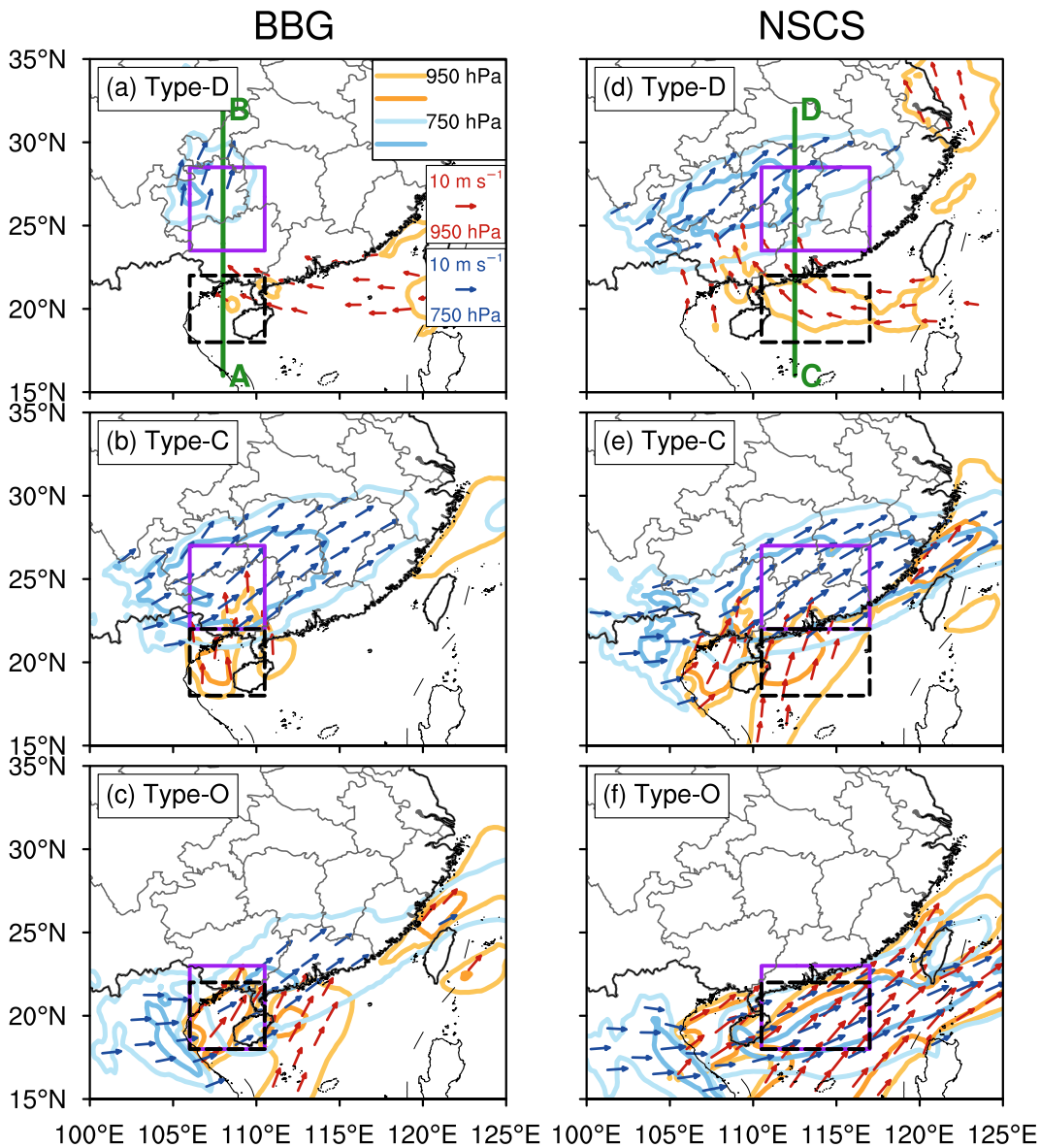

Figure 4. Composite distribution of horizontal wind speeds at 950 hPa (warm color contours of 10–12 m s^{-1} and red vectors) and 750 hPa (cold color contours of 10–12 m s^{-1} and blue vectors) for Type-D (a, d), Type-C (b, e), and Type-O (c, f) events in the BBG (a–c) and NSCS (d–f). Black (purple) boxes outline the main regions of the boundary layer jets (SLLJs) for the three double low-level jet types and will be referenced and discussed in Section 4.2.

Vertical cross-sections further reveal the intensity and relative positions of BLJs and SLLJs (Figure 5). In all three types, BLJs are located at 950 hPa over the ocean, while SLLJs are centered at 750 or 800 hPa. Type-C exhibits the strongest SLLJs, which are positioned on the windward slopes of the Nanling Mountains (Figures 5c and 5d). This positioning facilitates the SLLJs to cross the mountains. Compared to the 800-hPa SLLJs in BBG Type-C (Figure 5c), SLLJs in NSCS Type-C show a stronger wind core at 750 hPa (Figure 5d). In contrast, SLLJs in Type-D are situated north of the Nanling Mountains (Figures 5a and 5b), whereas those in Type-O are located over the ocean (Figures 5e and 5f).

3.3. Monthly and Diurnal Variations

Figure 6a presents the monthly variation in DLLJ occurrence frequency. DLLJs primarily occur from April to July during the warm season over South China. In the BBG, the frequency reaches its primary peak in April, with a

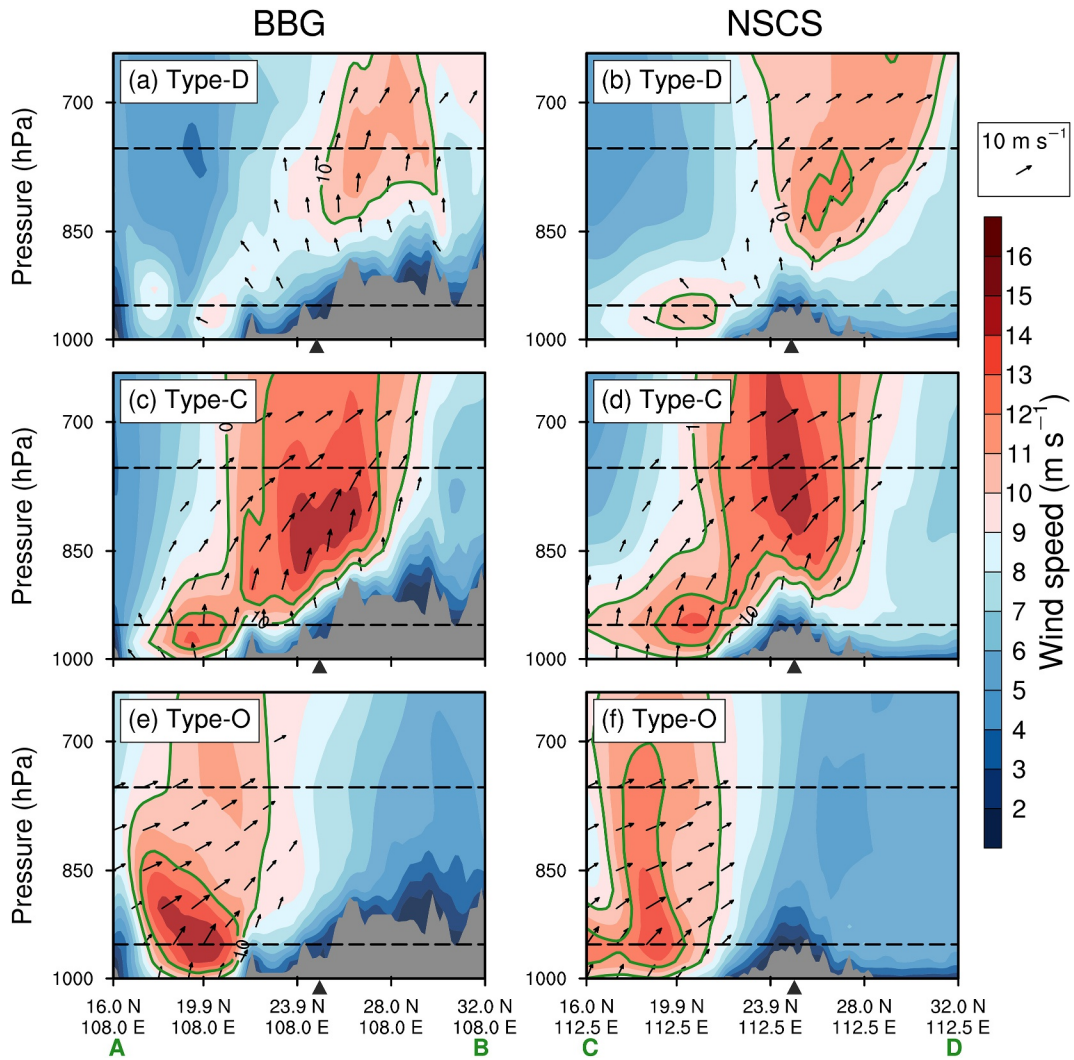

Figure 5. Vertical structures of horizontal wind speed (m s^{-1}, shading) and vectors (upward vectors indicate southerly winds) for Type-D (a, b), Type-C (c, d), and Type-O (e, f) events in the BBG (a, c, and e) and NSCS (b, d, and f) along the green lines A–B and C–D in Figures 4a and 4b, respectively. The two black dashed lines represent the 950-hPa and 750-hPa levels, respectively. The gray shading represents terrain and the black triangles mark the latitude of the Nanling Mountains (around 25°N).

secondary peak in June. In contrast, the NSCS features a major frequency peak in June. Figure 6b depicts the diurnal variation in DLLJ occurrence frequency. DLLJs exhibit a pronounced diurnal cycle, with a nocturnal peak between 0000 and 0500 LST. The peak over the BBG occurs at 0300 LST, while that over the NSCS is delayed by 2 hrs to 0500 LST. Notably, due to the 12-hr window of data assimilation in the ERA5 reanalysis, the occurrence frequency exhibits a decline between 1700 and 1800 LST in both regions. Moreover, a moderate DLLJ frequency persists during the daytime in both regions.

Figure 7 further shows the monthly distributions and diurnal cycles of the three DLLJ types. In terms of monthly variation, Type-D is most frequent in April and May over the BBG and the NSCS (Figures 7a and 7b). Type-C occurs primarily from April to June (Figures 7c and 7d). In the BBG, Type-C peaks in April (Figure 7c), whereas its peak in the NSCS is delayed to June (Figure 7d). Type-O occurs mainly from June to August (Figures 7e and 7f). The occurrence frequency of Type-O peaks in June over the BBG (Figure 7e) but shifts to July–August in the NSCS (Figure 7f). These pronounced seasonal differences and regional contrasts among DLLJ types may be attributed to the southward migration of mid-latitude westerly systems and the northward progress of monsoon flows (Du & Chen, 2019a; Li & Du, 2021; Zhou et al., 2022).

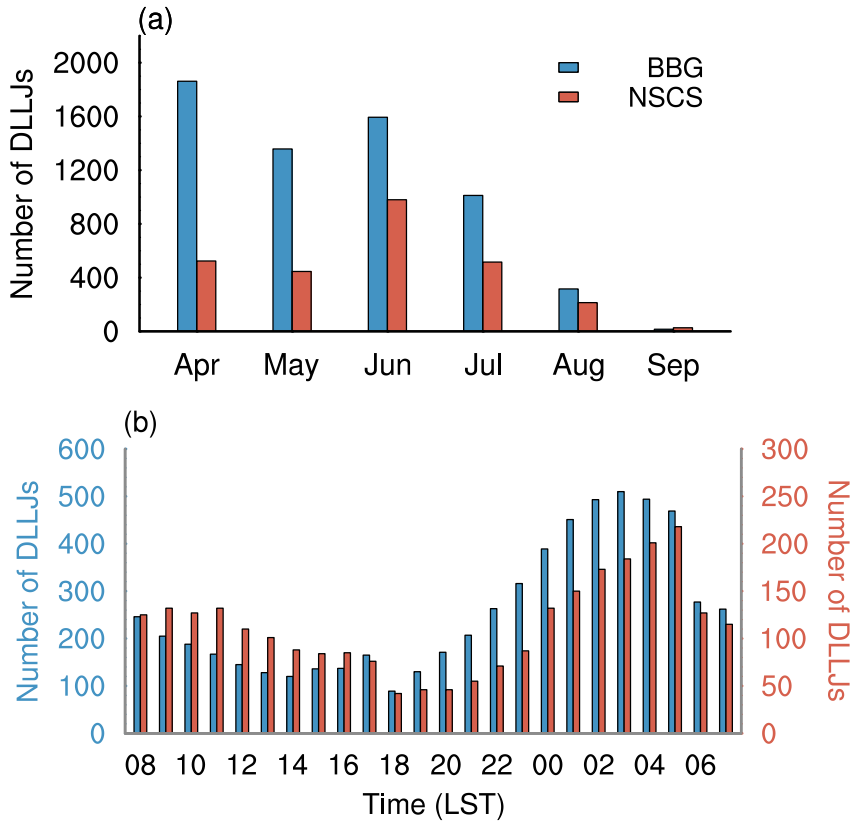

Figure 6. (a) Monthly variation in the number of double low-level jet (DLLJ) occurrences (counts) in the BBG and the NSCS. (b) Diurnal variation in the number of DLLJ occurrences (counts) during the warm season.

All three DLLJ types exhibit a nocturnal maximum in occurrence frequency. Additionally, Type-O in the BBG and Type-C/Type-O in the NSCS maintain a moderate frequency during the daytime (Figures 7d–7f). This pattern of diurnal variation may be associated with the relatively longer durations of these event types (Figures 3c and 3d). The physical processes underlying these diurnal features will be further examined in the following section.

4. Physical Processes Governing the Three DLLJ Types

4.1. Evolution of Synoptic Patterns

To examine the differences in synoptic-scale disturbances and their temporal evolution among the three DLLJ types, we composite 750-hPa geopotential heights, their corresponding anomalies, and wind fields, which are mainly associated with SLLJs. The composite time $t = 0$ hr is defined as the onset of each DLLJ event, with $t = -24$ hr and $t = +24$ hr denoting 24 hr before and after onset, respectively.

Figure 8 shows the evolution of synoptic systems at 750 hPa for the three DLLJ types in the BBG. Type-D events are characterized by the strengthening of the subtropical high, which extends from the western Pacific to South China between $t = -24$ hr and $t = +24$ hr (Figures 8a–8c). This subtropical high inhibits the southward migration of westerly disturbances from mid-high latitudes (Figure 8b), thereby forcing SLLJs to form northeast of the Yunnan-Guizhou Plateau and remain displaced from the marine BLJs. Type-C events are affected by an anomalous high-pressure system persisting over the South China Sea and an anomalous low-pressure system associated with the southwest vortex over the Sichuan Basin (Figures 8d–8f). From $t = -24$ hr to $t = 0$ hr, the intensifying low-pressure system enhances the land-sea pressure gradient (Figures 8d and 8e). This enhanced gradient facilitates the development of SLLJs over the southeastern Yunnan-Guizhou Plateau, where they partially overlap with marine BLJs. In contrast, Type-O events occur in the wake of a retreating high-pressure system, enabling westerly disturbances (land-based lows) to propagate into South China (Figures 8g–8i). This propagation not only intensifies the pressure gradient but also induces a near-complete overlap between SLLJs

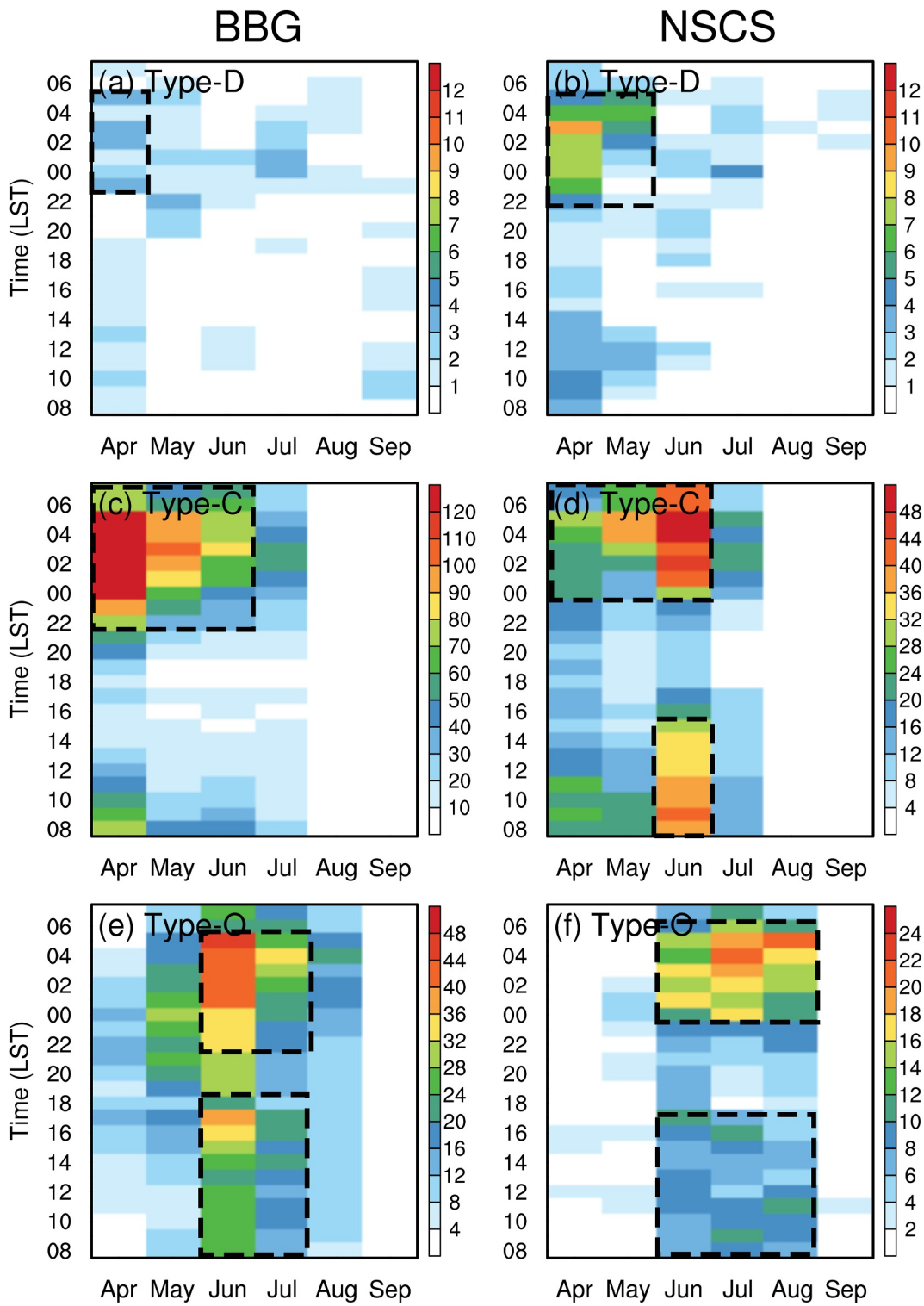

Figure 7. Monthly and diurnal variations in the occurrence frequency (counts) of three double low-level jet types in the BBG (a, c, and e) and the NSCS (b, d, and f).

and BLJs. Moreover, the weakening of the oceanic high-pressure system may facilitate the eastward and southward movement of westerly disturbances (Figures 8e vs. 8h), thereby triggering the sequential occurrence of Type-C followed by Type-O events (black boxes in Figure S2 of Supporting Information S1). Thus, diverse DLLJ

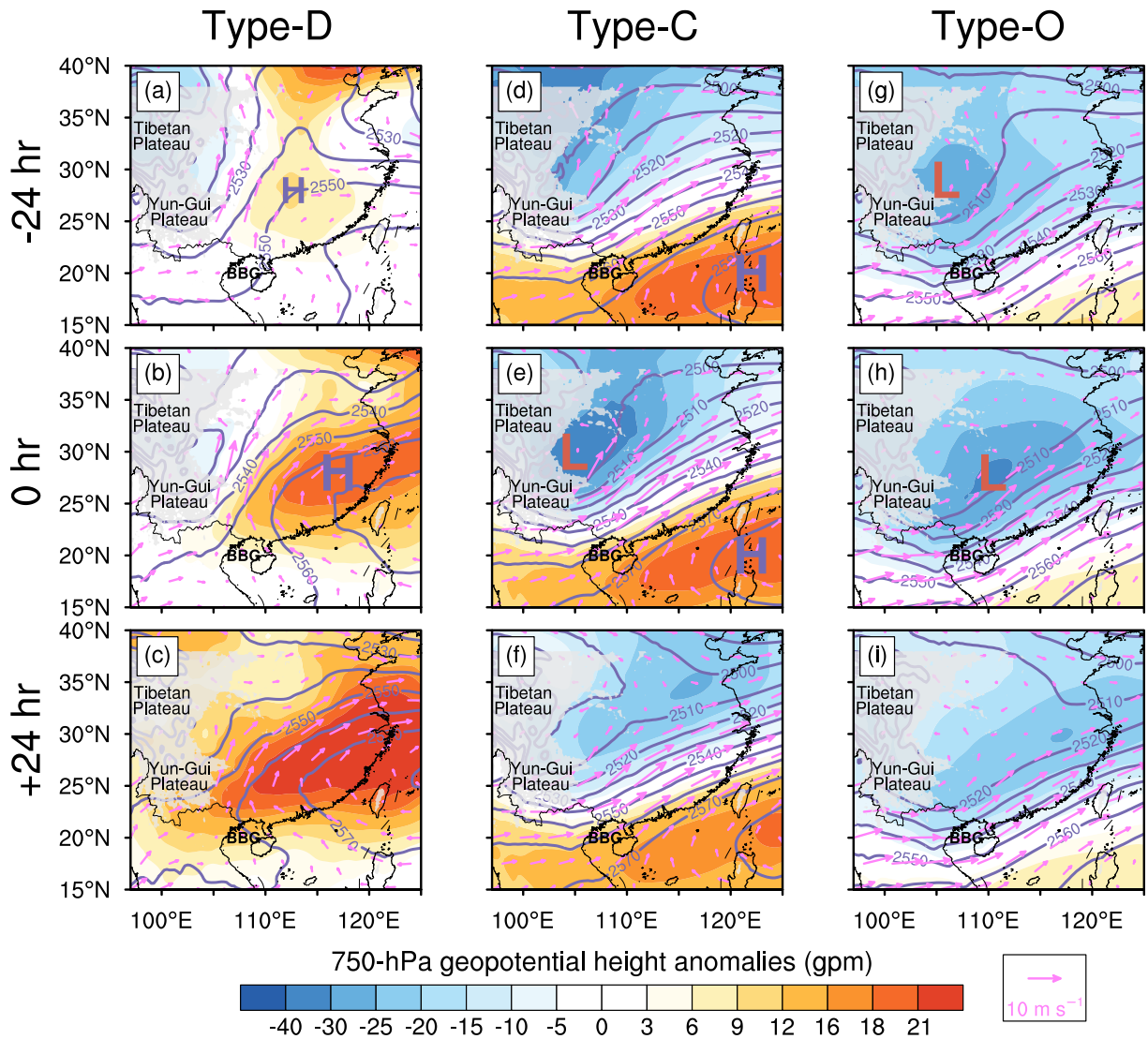

Figure 8. Composite 750-hPa geopotential height anomalies (shading, gpm), geopotential height (contoured every 10 gpm), and wind speeds (pink vectors, m s^{-1}) for (a–c) Type-D, (d–f) Type-C, and (g–i) Type-O in the BBG. The (top) −24 hr, (middle) 0 hr, and (bottom) +24 hr indicate the times corresponding to 24 hr before, at, and 24 hr after the onset of Type-D, Type-C, and Type-O events, respectively. The symbols "H" and "L" denote the centers of anomalous high-pressure systems and anomalous low-pressure systems, respectively. The geopotential height anomalies are calculated by subtracting the climatological mean geopotential height from April to September of 2001–2023.

structures are modulated by the position of westerly disturbances and the intensity of high-pressure systems. These synoptic configurations regulate the north–south positioning of SLLJs, thereby generating diverse coupling structures with marine BLJs.

Figure 9 illustrates the evolution of synoptic systems at 750 hPa for the three DLLJ types in the NSCS. Type-D events feature an anomalous high-pressure system over the South China Sea (Figures 9a–9c), which is located farther southwest compared with its counterpart over the BBG (Figure 9b vs. Figure 8b). As a result, the SLLJs extend to the northern area of the NSCS and exhibit stronger westerly components. Type-C events are influenced by an anomalous high-pressure system over the South China Sea (Figures 9d–9f), though this system is slightly weaker than its counterpart over the BBG (Figure 9e vs. Figure 8e). This weaker high-pressure system exerts less blocking effect on the movement of shear lines and low-pressure disturbances from the Sichuan Basin, enabling them to propagate farther southward (Figures 9d and 9e). By $t = 0$ hr, these low-pressure disturbances and the South China Sea high together form a north-low-south-high pressure dipole (Figure 9e), which contrasts sharply with the northwest–southeast dipole observed for Type-C events in the BBG (Figure 8e). This contrast explains

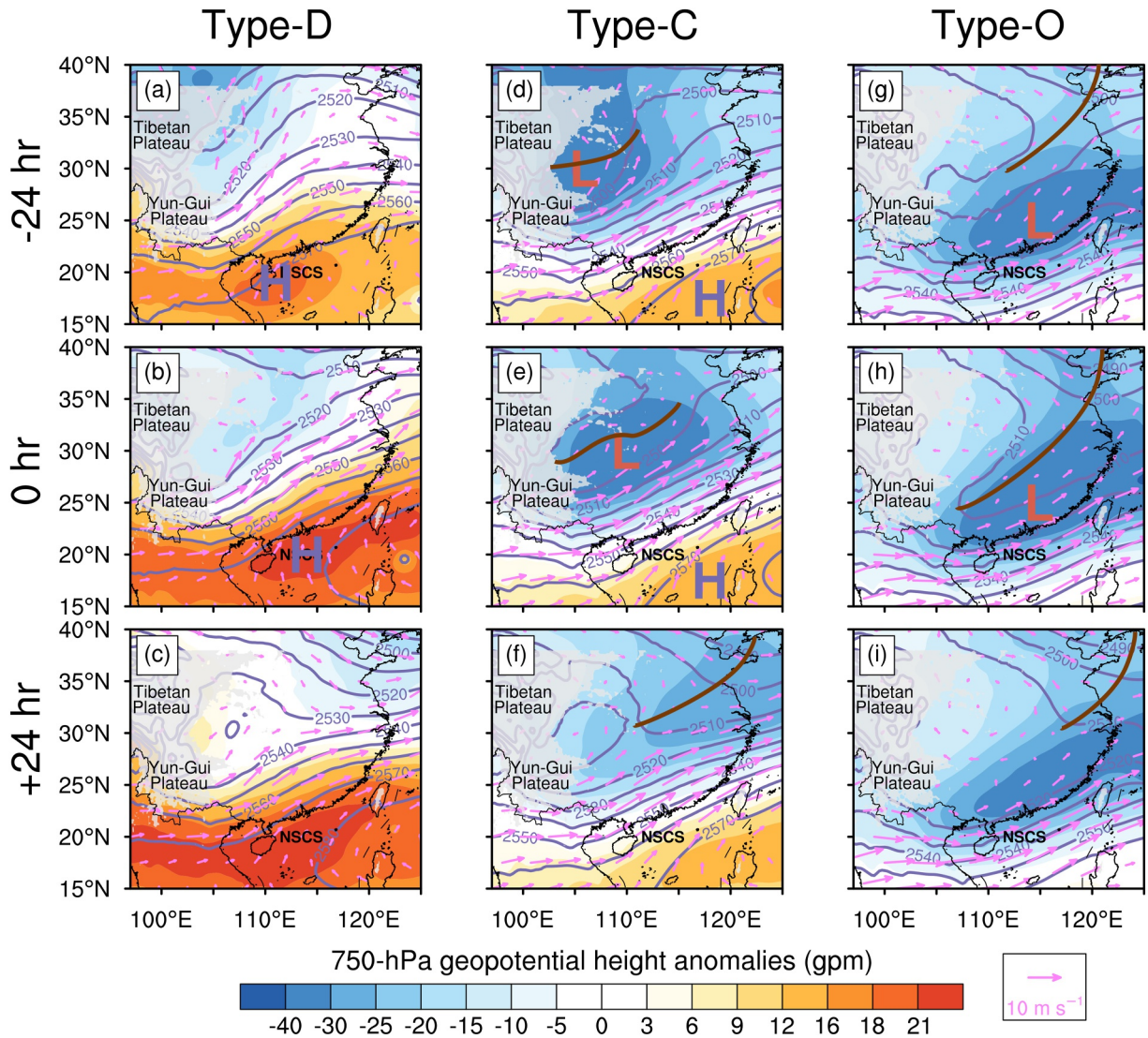

Figure 9. As shown in Figure 8, but for the NSCS. The brown bold lines indicate the shear lines and westerly troughs.

the more pronounced westerly component of SLLJs in Type-C events over the NSCS. Unaffected by high-pressure systems, Type-O events feature anomalous low-pressure systems extending to coastal areas, accompanied by the southward intrusion of mid-latitude westerly troughs (Figures 9g–9i). Over the NSCS, sustained pressure gradients drive southwesterly SLLJs that overlap with the marine BLJs.

Overall, the three DLLJ types are associated with varying synoptic disturbances. Type-D events feature dominant anomalous high-pressure systems over South China or the NSCS. Type-C events are affected by both anomalous low-pressure systems over land and high-pressure systems over the South China Sea. Type-O events are linked to land-based low-pressure anomalies. Moreover, circulation characteristics at 950 hPa (Figures S3 and S4 in Supporting Information S1) are analogous to those at 750 hPa, indicating that BLJs are also modulated by synoptic disturbances (Du & Chen, 2018; Luo & Du, 2023).

4.2. Governing Processes of Diurnal Variation

The occurrence frequencies of the three DLLJ types over the BBG and the NSCS exhibit obvious diurnal variations (Figure 7). This subsection further explores the detailed physical processes underlying these diurnal cycles of wind speeds in SLLJs and BLJs for each type, following the momentum balance method proposed by Du et al. (2014). The governing equation for meridional momentum balance is analyzed at 750 hPa (950 hPa) within

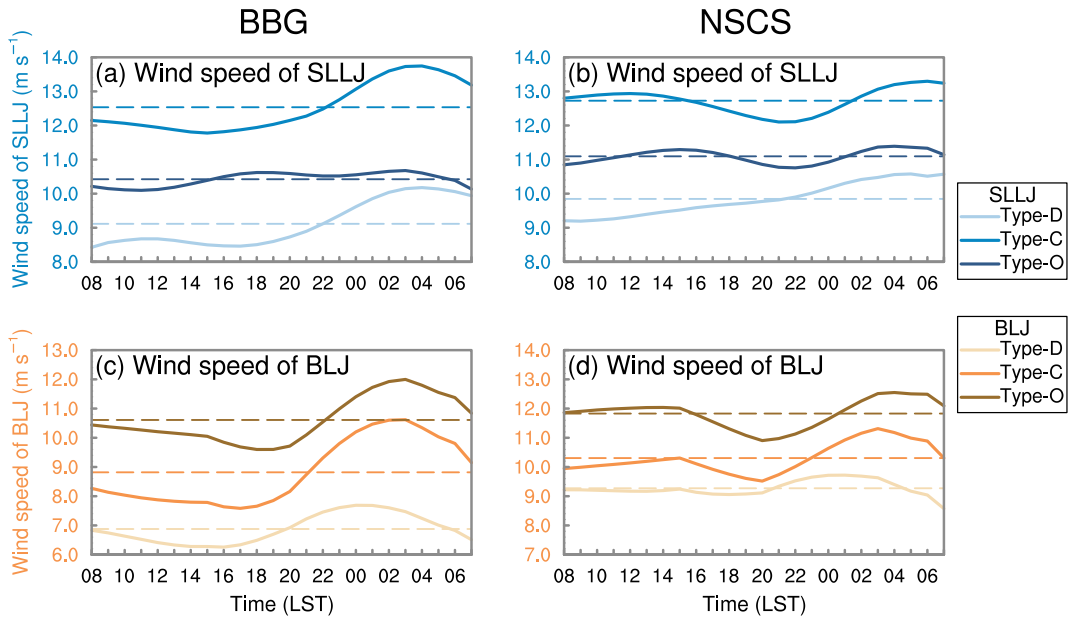

Figure 10. (a, b) Diurnal variations of average wind speeds (m s^{-1}) at 750 hPa in the purple boxes in Figure 4 for the three types of double low-level jet in the BBG and the NSCS. Panels (c, d) same as (a, b), but for 950 hPa in the black dashed boxes in Figure 4. To minimize the impact of the 12-hr assimilation window in the ERA5 reanalysis, a five-point running average was applied to smooth the time series.

the purple boxes (black dashed boxes) in Figure 4. The coordinate system is defined as follows: The *y*-axis aligns with the direction of daily mean wind, and the *x*-axis is perpendicular to the *y*-axis toward the right.

$$\frac{\partial v}{\partial t} = \left(-u\frac{\partial v}{\partial x} - v\frac{\partial v}{\partial y}\right) - \frac{\partial \varnothing}{\partial y} - fu + F_y$$

TD HAD PGF CF Fr

where the terms represent local acceleration (TD), horizontal advection, pressure gradient force (PGF), Coriolis force (CF), and frictional/residual terms (Fr). The vertical advection is neglected here due to its minor contribution.

Figure 10 depicts the diurnal variations in wind speed at 750 hPa (SLLJs) and 950 hPa (BLJs) for the three DLLJ types. For SLLJs, Type-D and Type-C exhibit a prominent nocturnal wind maximum: the wind speed peaks at ~0300 LST for BBG events (Figure 10a) and ~0500 LST for NSCS events (Figure 10b). In contrast, Type-O events show relatively minimal diurnal cycles, featuring wind speed increases at night and in the afternoon. Moreover, a morning increase in wind speed is also present in Type-C events over the NSCS. For BLJs, all types display pronounced nocturnal maxima, with the peak timing of Type-D events preceding that of Type-C and Type-O events by about 2 hrs (Figures 10c and 10d).

Figure 11 depicts the momentum budget analysis for 750-hPa (SLLJs) and 950-hPa (BLJs) winds across the three DLLJ types. The analysis elucidates the diurnal wind variations by evaluating the contributions of the PGF (driving force), Fr (dissipative force), and CF (deflective force). For 750-hPa SLLJs, the PGF shows a semi-diurnal pattern with daytime and nighttime peaks in all types (blue lines in Figures 11a–11f), which is driven by the semi-diurnal cycle of pressure tides (Huang et al., 2010; Lindzen & Chapman, 1969). For Type-D and Type-C events, Fr is strongly negative during the daytime due to enhanced surface heating and turbulent mixing over land, and it weakens at night (gray lines in Figures 11a, 11b, 11d, and 11e). In contrast, Type-O events (marine SLLJs) maintain near-zero Fr throughout the day (Figures 11c and 11f), which is attributed to the inherently lower boundary-layer height over the ocean. The CF term undergoes a phase reversal, negative during the daytime and positive at night (purple lines in Figures 11a–11f), indicative of inertial adjustment in response to large-scale land-sea thermal contrasts (Du, Rotunno et al., 2015; Du, Chen et al., 2015). Therefore, the nocturnal

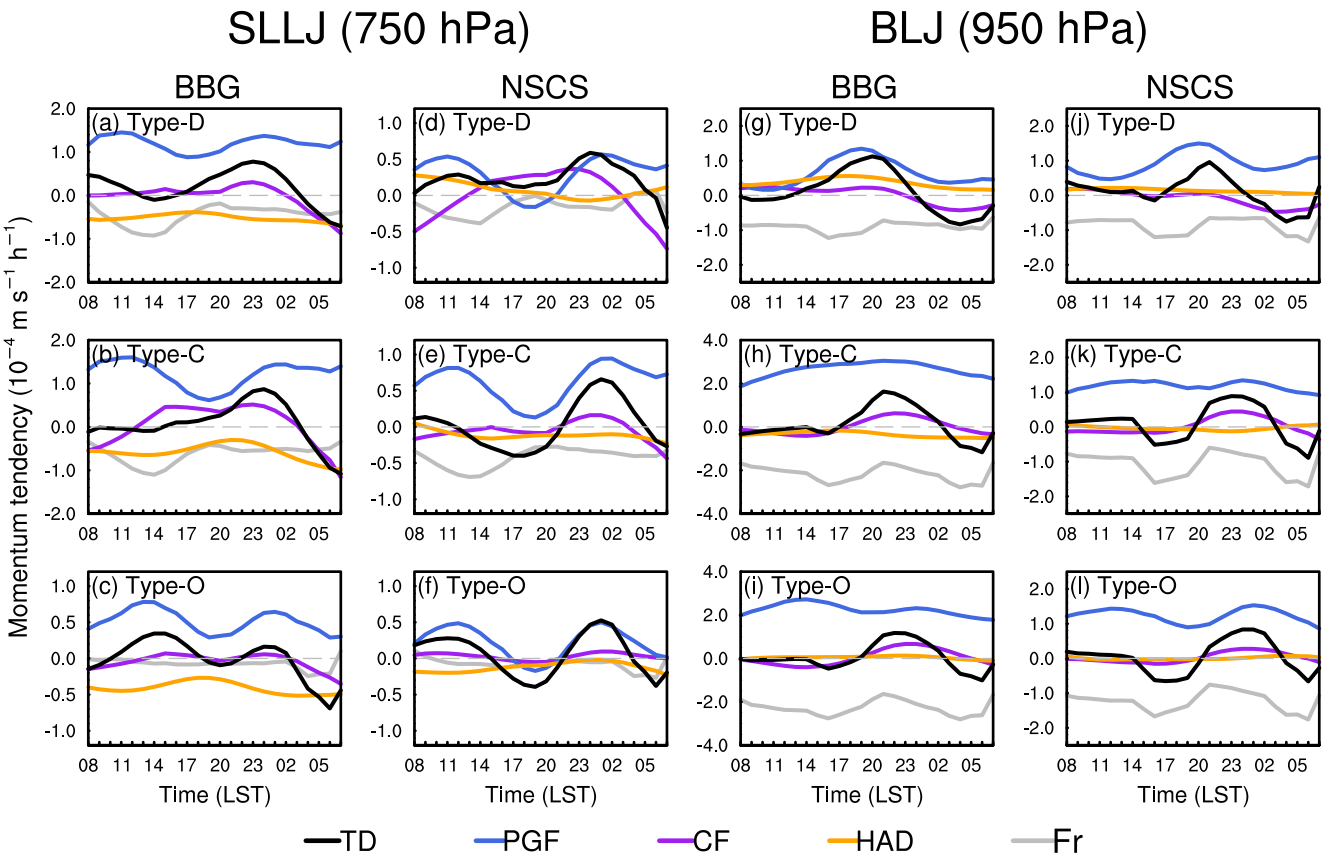

Figure 11. (a–f) Diurnal variations of each term (10^{-4} m s^{-1} hr^{-1}) in the horizontal momentum equation at 750 hPa averaged over the purple boxes in Figure 4, respectively. (g–l) Diurnal variations of each term (10^{-4} m s^{-1} hr^{-1}) in the horizontal momentum equation at 950 hPa averaged over the black dashed boxes in Figure 4. To minimize the impact of the 12-hr assimilation window in the ERA5 reanalysis, a five-point running average was applied to the data.

acceleration of SLLJs is mainly due to an increase in PGF combined with reduced turbulent friction, with CF exerting an indirect influence. During the daytime, strong friction over land (Type-D/C) counteracts the daytime PGF peak, suppressing wind acceleration. Over the ocean (Type-O), sustained weak friction allows both daytime and nighttime PGF peaks to effectively accelerate winds.

For 950-hPa BLJs (Figures 11g–11l), the PGF is consistently positive, with a less prominent semi-diurnal signal than that of the 750-hPa PGF (blue lines; Figures 11g–11l vs. Figures 11a–11f). The Fr term not only exhibits greater negative magnitudes than at 750 hPa but also weakens after sunset (gray lines; Figures 11g–11l vs. Figures 11a–11f). The CF term follows a trend analogous to that at 750 hPa (purple lines in Figures 11g–11l). Thus, the nocturnal acceleration of BLJs mainly results from the combined effects of enhanced PGF from pressure tides and weakened friction. The earlier peak in Type-D events arises from southeasterly background flows, which shorten the time for ageostrophic winds to rotate clockwise and align with the background winds via inertial oscillations (Figure S5; Blackadar, 1957). In addition, Type-D exhibits a weaker 950-hPa nocturnal enhancement than Type-C and Type-O. This is consistent with prior findings that small nocturnal wind enhancements are correlated with weak background flows (Chen, 2020; Shapiro et al., 2016).

Overall, all BLJs and SLLJs exhibit nocturnal wind maxima, primarily driven by the combined effects of enhanced PGF from pressure tides and weakened friction at night. For Type-O, marine SLLJs show an afternoon increase in wind speed, as weak oceanic friction at 750 hPa fails to offset daytime acceleration from pressure tides. Previous studies have mainly emphasized the impact of boundary-layer thermal effects on the diurnal BLJ variations (Du & Rotunno, 2014). Our findings highlight the critical role of semi-diurnal pressure tides in driving PGF variations, particularly for SLLJs at higher elevations. We further clarify that the competition between the PGF from pressure tides and the friction governs the diurnal variation of LLJs over both oceanic and continental regions.

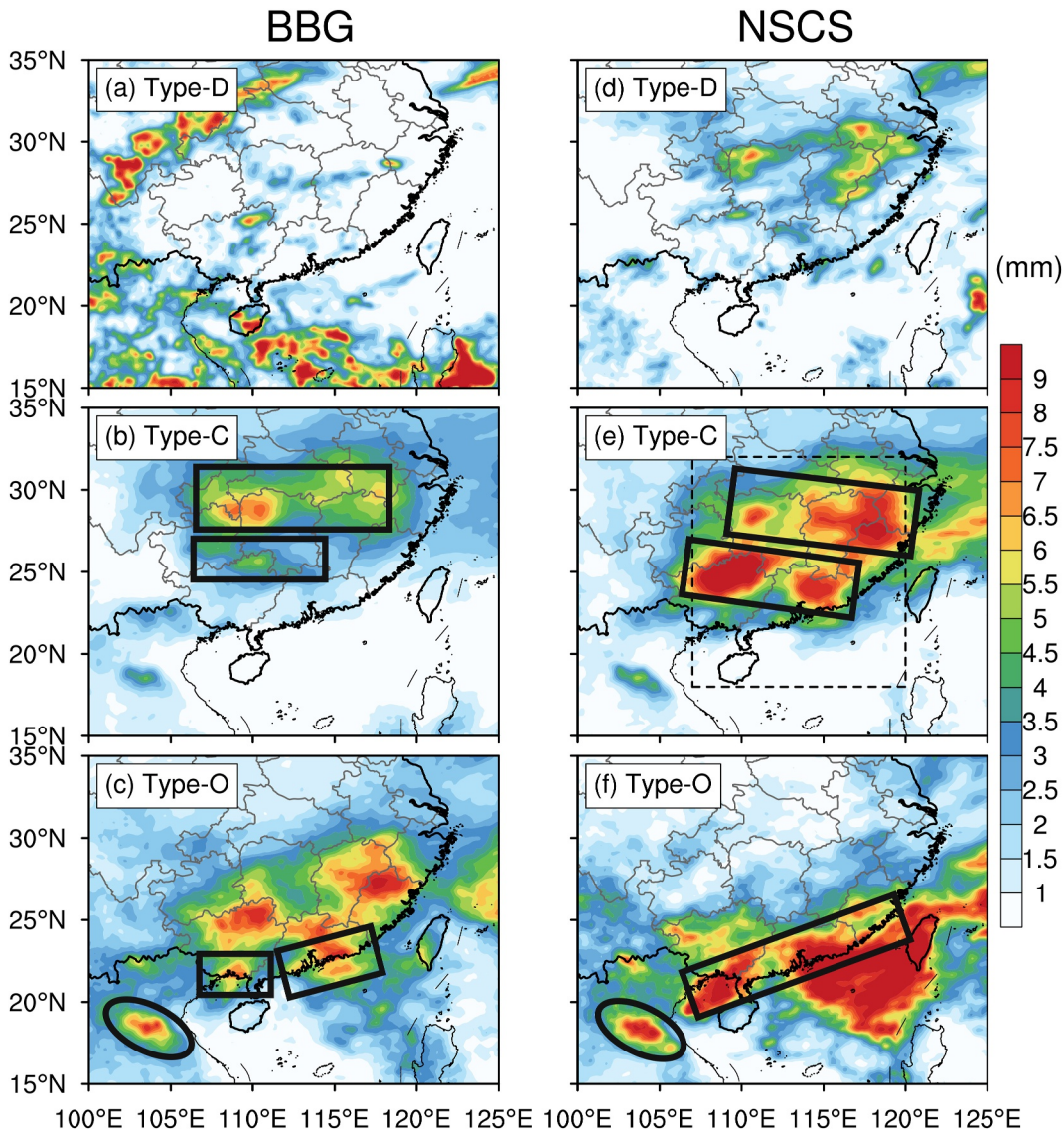

Figure 12. Composite rainfall accumulated within 9 hr after the onset of (a) Type-D, (b) Type-C, and (c) Type-O events (shading, mm) in the BBG. Panels (d–f) are same as (a–c) but in the NSCS.

5. The Impact of DLLJs on Precipitation

During the active phases of DLLJs, precipitation in South China is obviously enhanced, forming two east-west-oriented rainbands (Figures 1b and 1c; Li & Du, 2021). In this section, we further explore how variations in DLLJ structures impact rainfall patterns.

5.1. Rainfall Patterns Associated With Three DLLJ Types

Figure 12 shows the rainfall patterns of the three types of DLLJ events. In the BBG, Type-D events exhibit rainfall centered over the Sichuan Basin, with weak rainfall in southern China (Figure 12a). In contrast, Type-C events generate an east-west-oriented rainband along 28°N in the Yangtze River Basin, along with weaker rainfall at the south of Nanling Mountains (Figure 12b). For Type-O events, rainfall is concentrated south of the Nanling Mountains and west of the Wuyi Mountains, with enhanced coastal rainfall along the coast of South China (Figure 12c).

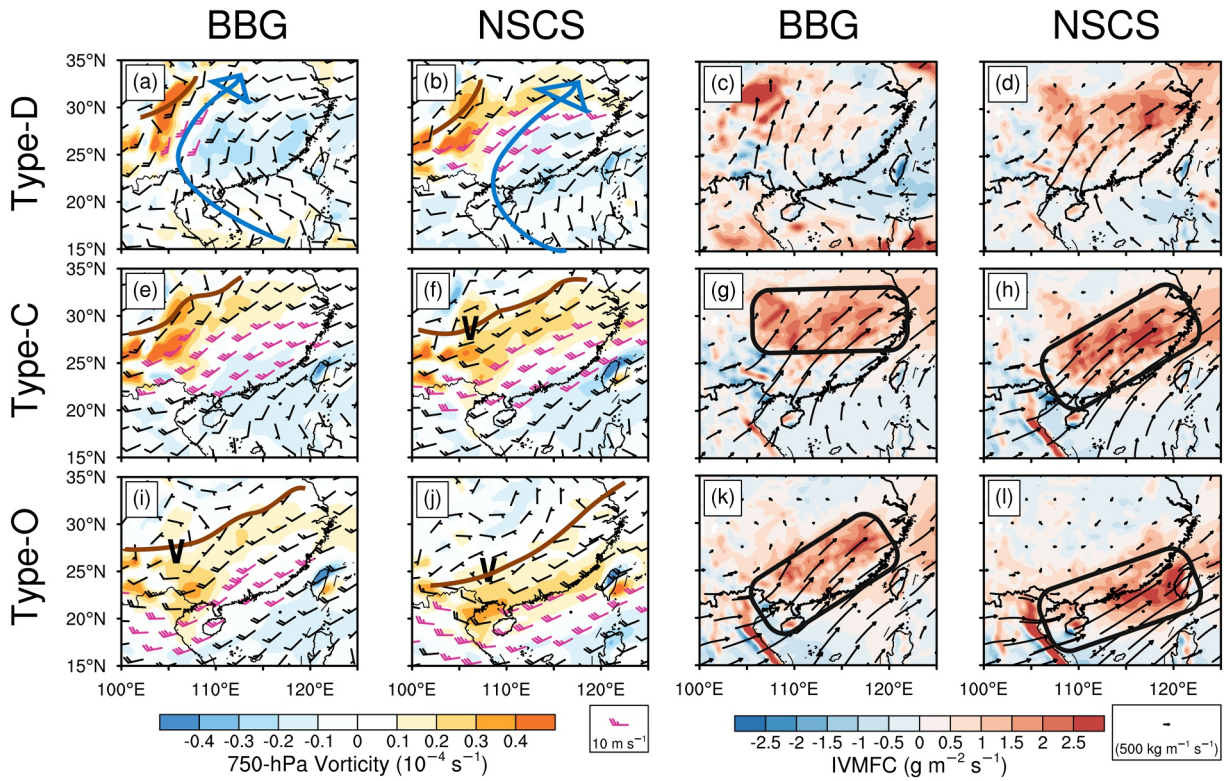

Figure 13. (a, b, e, f, i, and j) Composite of 750-hPa vorticity (shading, 10^{-4} s^{-1}) and horizontal wind speeds (m s^{-1}) averaged within 9 hr after the onset of (a, b) Type-D, (e, f) Type-C, and (i, j) Type-O events in the BBG (a, e, and i) and the NSCS (b, f, and j). The "V" symbols denote low vortices. The brown lines indicate shear lines, and the blue arrows represent anticyclonic circulations. (c, d, g, h, k, and l) Composite of integrated vertical moisture flux convergence (shading, g m^{-2} s^{-1}) and moisture flux (vectors, 500 kg m^{-1} s^{-1}) from the surface to 600 hPa for (c, d) Type-D, (g, h) Type-C, and (k, l) Type-O events in the BBG (c, g, and k) and the NSCS (d, h, and l).

In the NSCS, Type-D events produce scattered rainfall centers in the Yangtze River Basin (Figure 12d), likely due to the coexistence of Type-D (NSCS) and Type-C (BBG), as will be discussed in Section 6. Type-C events feature two prominent east-west-oriented rainbands: one north of the Nanling-Wuyi mountains and another south of the Yunnan-Guizhou Plateau and Nanling Mountains (Figure 12e). Compared to the rainbands of Type-C events in the BBG, these two rainbands are slightly south-shifted and exhibit greater intensity (Figures 12b vs. 12e). For Type-O events, rainfall is concentrated along the South China coast and adjacent marine areas (Figure 12f), while rainfall in central China is suppressed. Notably, Type-O events in both regions trigger anomalous rainfall in northern Vietnam (18.5°N, 104°E). This is likely due to orographic lifting, as airflow over the Indochina Peninsula crosses the Annamite Mountains (Kong et al., 2020).

Overall, Type-D events yield the weakest rainfall in southern China, with their rainbands situated farthest north. Type-C events generate two east-west-oriented rainbands flanking the Yunnan-Guizhou Plateau and Nanling Mountains, while Type-O events notably affect rainfall along South China's coast, underscoring their critical role in regional hydrometeorological processes.

5.2. Circulation Patterns and Moisture Transport

Figure 13 depicts 750-hPa circulation patterns mainly related to SLLJs and integrated vertical moisture flux convergence (IVMFC, surface–600 hPa) associated with DLLJs. Type-D events are characterized by a dominant anticyclonic circulation in South China, creating an environment, that is, unfavorable for rainfall (Figures 13a and 13b). For the BBG, Type-D events involve moisture advection along the northwestern edge of the anticyclone and meridional wind shear near the Sichuan Basin (Figures 13a and 13c). Collectively, these factors drive localized rainfall in the Sichuan Basin. For the NSCS, Type-D events are marked by a slight southward movement of the anticyclonic circulation (Figure 13b), which in turn shifts the water vapor convergence center to the lower Yangtze River reaches (Figure 13d).

Type-C events exhibit anticyclonic flow over the NSCS in conjunction with an intensified shear line in the Yangtze River Basin (Figures 13e and 13f). For the BBG, enhanced winds south of the shear line facilitate moisture transport from the South China Sea to the Yangtze River Basin, thereby forming a robust east-west oriented moisture convergence zone (Figures 13e and 13g). For the NSCS, the shear line in Type-C events shifts further south and extends eastward to the middle reaches of the Yangtze River, promoting the development of a closed low vortex (Figure 13f). To the south of this shear line, enhanced convergence gives rise to a prominent moisture convergence zone aligned in a southwest–northeast direction (Figures 13f and 13h).

Type-O events feature a shear line that shifts southward and stretches, accompanied by an intensified closed low vortex (Figures 13i and 13j). Along the coast of South China, a cyclonic circulation with positive vorticity forms, triggering coastal rainfall. In the BBG, the low-vortex center extends to the northern boundary of Guangxi Province, with strong southwesterly coastal flows exceeding 10 m s^{-1} (Figure 13i). These flows drive enhanced moisture convergence from the ocean to the western foothills of the Wuyi Mountains (Figure 13k), which is attributed to the coupling of marine BLJs and northeastward-extending SLLJs. In the NSCS, the low vortex and shear line in Type-O events shift southward to central Guangxi Province, generating a coastal cyclonic circulation (Figure 13j). Moreover, moisture transport from LLJs over the NSCS leads to enhanced rainfall along the coast and adjacent coastal areas (Figure 13l).

These differences in moisture convergence and vorticity align well with the rainfall patterns of the three DLLJ types. Rainfall is jointly modulated by both DLLJs and synoptic disturbances. Marine BLJs regulate the intensity of moisture transport, with stronger marine jets transporting more moisture from the ocean to the land. The meridional movement of SLLJs, which is driven by shifts in shear lines, further regulates the north–south positioning of moisture convergence zones. Moreover, the coupling of low-level vortices and LLJs enhances convergence, thereby boosting local rainfall intensity.

5.3. Convergent Lifting Under Three DLLJ Types

Figure 14 further presents latitude-vertical cross-sections of divergence, vertical motion, and meridional wind for the three DLLJ types in the BBG and NSCS. In Type-D events, low-level convergent flow and upward motion are the weakest (Figures 14a and 14b), resulting in suppressed rainfall due to insufficient dynamical lifting. For Type-C events, strong southerly BLJs impinge on the Nanling Mountains, which generate intense boundary-layer convergent lifting (1,000–900 hPa) on the windward slopes (Figures 14c and 14d). Meanwhile, downward motion occurs on the leeward side, with secondary upward motion forming downstream of this subsidence zone (Figures 14c and 14d). The dual rainbands associated with Type-C events can thus be attributed to the hydraulic jump effect (Rotunno & Bryan, 2018). On the windward side, convergence in the BLJ exit region couples with mid-level (900–700 hPa) divergence in the SLLJ entrance region, producing mesoscale lifting that favors convective initiation. In addition, windward lifting in Type-C events over the BBG is weaker than that over the NSCS, likely owing to a lower SLLJ core level (800 hPa, Figure 5c) and reduced convergence intensity. On the leeward side, rainfall is associated not only with shear line convergence but also with hydraulic jump lifting induced by the elevated SLLJs crossing the mountains. Moreover, in Type-C events over the NSCS, rainfall on the eastern side of the northern rainband is obviously enhanced (Figure 12e), which may be linked to the orographic lifting on the windward side of the Wuyi Mountains, induced by westerly SLLJs impinging on the range (Figure 14d). In contrast, Type-O events feature pronounced low-level convergence and upward motion near the windward slopes of mountains and coastal zones (Figures 14e and 14f). In the BBG, Type-O events exhibit moderate convergent uplift on the leeward slopes (Figure 14e), driven by interactions between the northeastward-extending SLLJs and the western flank of the Wuyi Mountains. These results highlight that DLLJs strongly modulate regional rainfall through convergence/divergence and low-level lifting that depend on wind structures and local terrains.

6. The Relationship Between DLLJs in the BBG and the NSCS

Analyses shown in the preceding sections indicate that the occurrence of DLLJs is closely related to the positioning of synoptic disturbances. As westerly disturbances move southward, different DLLJ types may occur concurrently or sequentially in the BBG and NSCS. In this section, we use conditional probability to examine the various types of DLLJs that occur jointly in the two regions, so that we can clarify how the regional DLLJs develop with the moving westerly disturbances.

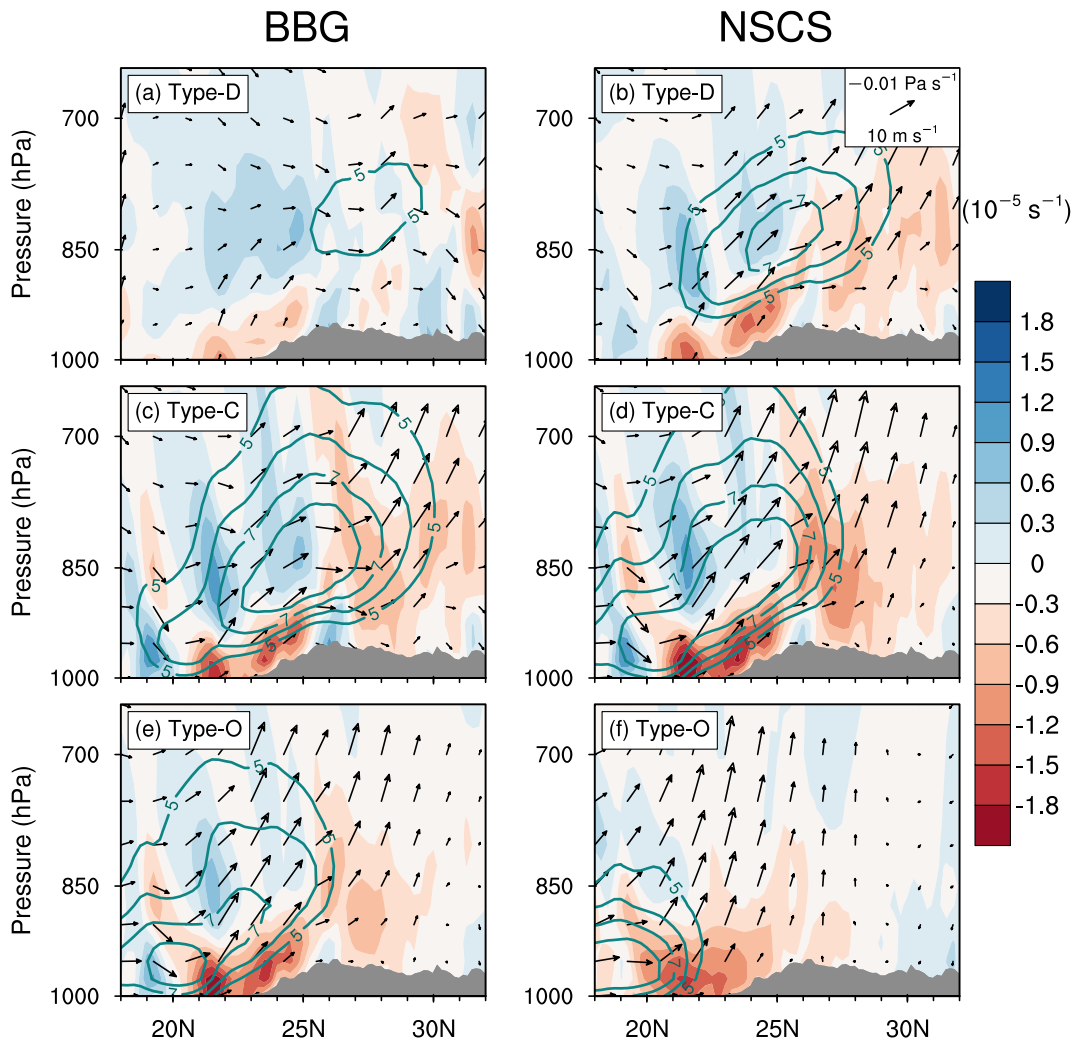

Figure 14. Latitude-vertical cross-sections of the composite divergence (shading, 10^{-5} s^{-1}), meridional wind (contours and vectors, m s^{-1}) and vertical motion (vectors: −0.01 Pa s^{-1}) averaged over 105°–120°E within 9 hr after the onset of (a, b) Type-D, (c, d) Type-C, and (e, f) Type-O events in the BBG (a, c, and e) and the NSCS (b, d, and f). The gray shading represents terrain.

Figure 15 shows the conditional probabilities of the three DLLJ types in the BBG when any given DLLJ type occurs in the NSCS. When Type-D events appear in the NSCS, Type-C events in the BBG have a high occurrence probability of 39.3%. The synoptic pattern is characterized by a low vortex northwest of the Nanling Mountains and an anticyclone over the South China Sea (Figure 16a). When Type-C events occur in the NSCS, the occurrence probabilities of Type-C and Type-O events in the BBG are 22.8% and 18.3%, respectively. For the joint occurrence of NSCS Type-C and BBG Type-C, the anticyclone over the South China Sea moves southward, while the low vortex accompanied by a shear line shifts southward with a slight eastward movement (Figure 16b). For the joint occurrence of NSCS Type-C and BBG Type-O, the anticyclone over the South China Sea retreats further eastward, and the low vortex related to the shear line migrates southward to the vicinity of the Nanling Mountains (Figure 16c). When Type-O events appear in the NSCS, Type-O events in the BBG have a high occurrence probability of 31%. In this situation, the NSCS is not affected by the anticyclone, allowing westerly disturbances to propagate further southward to the southern region of the Nanling Mountains (Figure 16d). Overall, the BBG has a smaller distance from westerly disturbances (i.e., low vortices), leading to an earlier phase of transition between different DLLJ types compared with that in the NSCS.

Figure 16 further presents rainfall distributions for coexisting DLLJs in these two regions. For the joint occurrence of NSCS Type-D and BBG Type-C, rainfall is relatively weak and located in the Yangtze River Basin

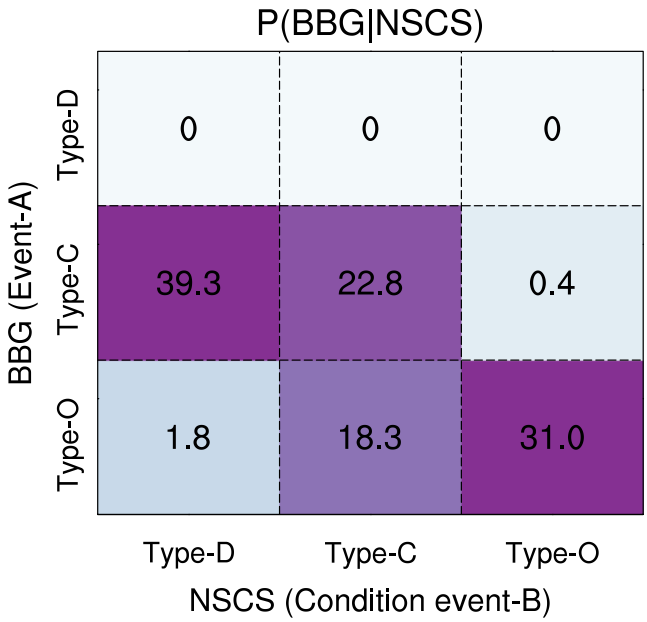

Figure 15. The conditional probabilities (%) of the three double low-level jet (DLLJ) types in the BBG when any given DLLJ type occurs in the NSCS.

(Figure 16a). When NSCS Type-C and BBG Type-C occur concurrently, rainfall in the Yangtze River Basin intensifies obviously (Figure 16b), which is probably attributed to the hydraulic jump of SLLJs. Meanwhile, weak rainfall also occurs on the windward slope of the Nanling Mountains (Figure 16b). This rainfall pattern is similar to that of NSCS Type-C and BBG Type-C (Figures 12b and 12e), with its intensity slightly weaker than that of NSCS Type-C but stronger than that of BBG Type-C.

For the coexistence of NSCS Type-C and BBG Type-O, the rainband over the Yangtze River Basin exhibits a marked enhancement and a further southeastward shift, extending to the northern flank of the Nanling-Wuyi Mountains (Figure 16c). This enhancement may be related not only to the hydraulic jump of SLLJs but also to orographic lifting by the Wuyi Mountains. In addition, rainfall is also markedly enhanced on the southern sides of the Nanling Mountains (Figure 16c), probably due to orographic lifting and mesoscale uplift induced by BLJ-SLLJ coupling. This rainfall pattern is comparable to that observed for NSCS Type-C and BBG Type-O (Figures 12c and 12e). For the joint occurrence of NSCS Type-O and BBG Type-O, rainfall is concentrated in the southern area of the Nanling Mountains (Figure 16d). This distribution arises from the combined effects of deep-layer convergence from overlapping BLJs and SLLJs, as well as coastal orographic lifting. Thus, the concurrent presence of DLLJs in these two regions leads to a linear superposition of the rainfall patterns that correspond to each DLLJ type.

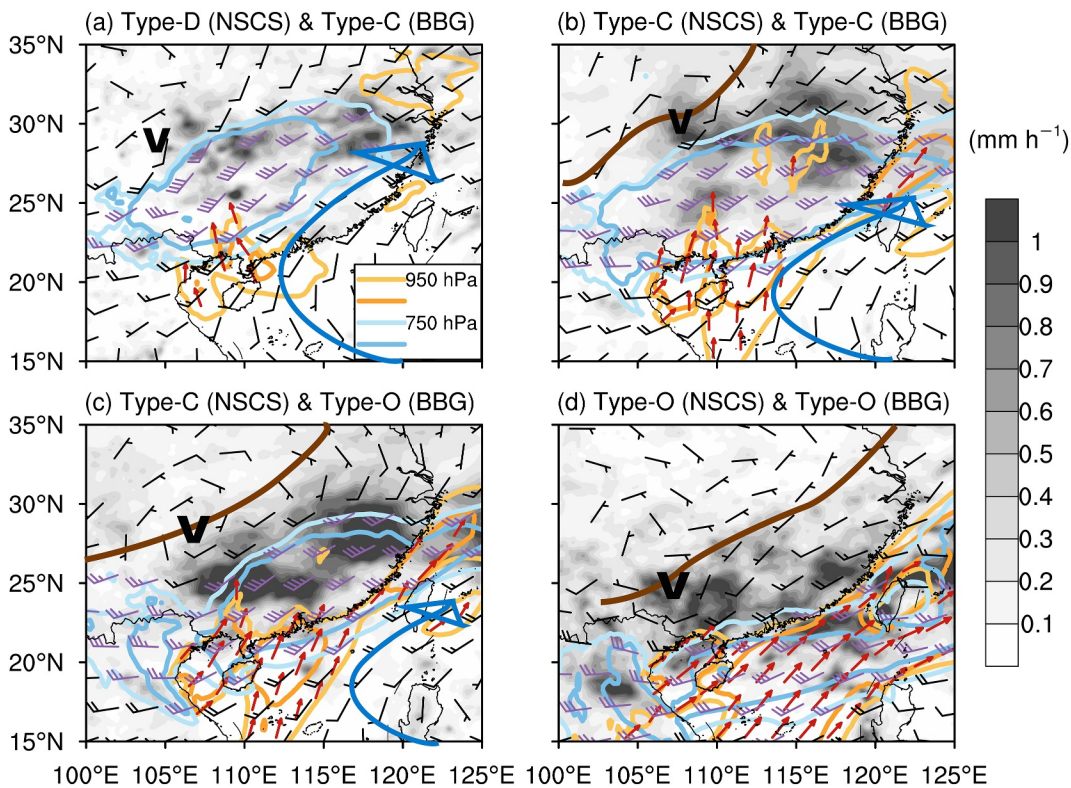

Figure 16. Composite distributions of mean rainfall rate (shading, mm h^{-1}), horizontal wind speeds at 950 hPa (warm color contours of 10–12 m s^{-1} and red vectors) and 750 hPa (cold color contours of 10–12 m s^{-1} and purple/black barbs) when double low-level jets occur simultaneously in the BBG and NSCS. The "V" symbols denote low vortices. The brown lines indicate shear lines, and the blue arrows represent anticyclonic circulations.

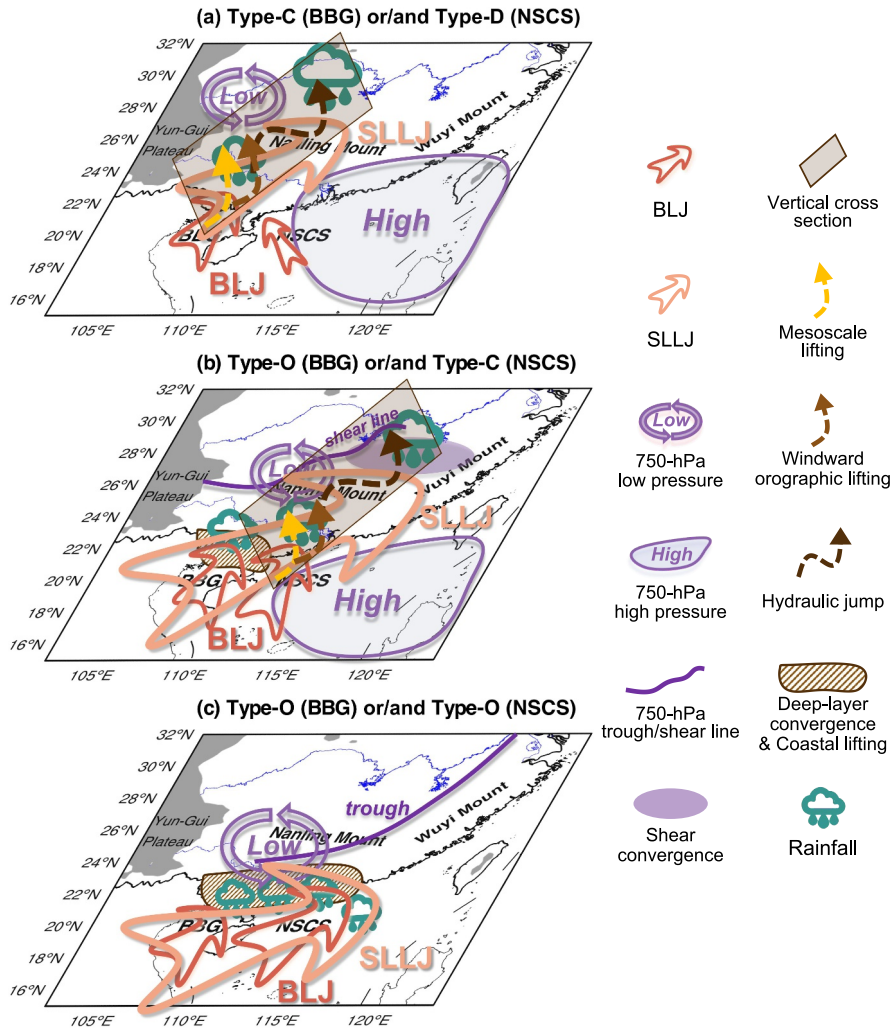

Figure 17. Schematic diagrams of the favorable synoptic disturbances and rainfall patterns for the three groups of double low-level jet (DLLJ) events in the BBG and the NSCS. These three groups are chosen based on their relatively high occurrence frequencies, as shown in Figure 15. Type-D events in the BBG are not shown here, as they are few in number and do not co-occur with DLLJs in the NSCS.

7. Conclusions and Discussions

Low-level jets (LLJs) in South China exhibit diverse structures, and are typically classified into BLJs and synoptic-system-related low-level jets (SLLJs) based on the height of their maximum wind speed. BLJs primarily occur over offshore regions such as the Beibu Gulf (BBG) and the northern South China Sea (NSCS), while SLLJs form over land and propagate with synoptic disturbances. When BLJs and SLLJs coexist in a region, they form DLLJs. This study investigates the structural diversity of DLLJs and their impacts on rainfall during the warm season (April–September), using 23 years of ERA5 reanalysis and IMERG rainfall data. The study focuses on the BBG and the NSCS, and their adjacent northern landmasses. The main findings are illustrated in Figure 17 and are summarized as follows:

DLLJs occur in three coupling patterns: Displaced (Type-D, comprising 3% of all DLLJ events) with no horizontal overlap between BLJs and SLLJs; Connected (Type-C, 66%) with partial horizontal overlap; and Overlapped (Type-O, 31%) with nearly coincident cores. The intensity of BLJs increases as the horizontal distance from SLLJs decreases (Type-D < Type-C < Type-O), suggesting that the southward propagation of synoptic

disturbances may enhance the marine BLJs. BLJs in Type-D are dominated by southeasterly winds, whereas both BLJs and SLLJs in Type-C and Type-O are southwesterly winds.

The three DLLJ types exhibit different monthly variations in occurrence frequency, associated with various synoptic disturbances. Type-C events mainly occur from April to June, driven by the interaction between anomalous low-pressure systems over land and anomalous high-pressure systems over the South China Sea. In the BBG, Type-C is shaped by developing southwest vortices and South China Sea high pressures, forming a northwest-southeast dipole. In the NSCS, Type-C is affected by the coupling of low-pressure disturbances associated with shear lines and the South China Sea high pressures, creating a north-low-south-high dipole. Type-O events mainly occur from June to August south of land-based low-pressure anomalies. In the BBG, they are affected by the southward movement of an anomalous low-pressure system, while in the NSCS, they emerge from coastal anomalous low-pressure systems coupled with southward intrusions of mid-latitude westerly troughs. Type-D events are confined to April–May along the western/northern flanks of high-pressure anomalies.

The occurrence frequency of DLLJs features a pronounced diurnal cycle, with a primary nocturnal peak between 0000 and 0500 LST. The peak occurs earlier in the BBG (0300 LST) and later in the NSCS (0500 LST), respectively. All three DLLJ types exhibit a nocturnal maximum in occurrence frequency. Momentum budget analysis reveals that both BLJs and SLLJs strengthen at night due to enhanced PGF from pressure tides combined with weakened frictional forces. In Type-O, SLLJs also exhibit an afternoon increase in wind speed, as weak oceanic friction at 750 hPa fails to counteract the daytime acceleration induced by pressure tides.

DLLJs strongly modulate rainfall patterns through low-level lifting that depends on wind structures and local terrains. Type-C generates two major rainbands: one on the windward (southern) side of the Nanling Mountains, driven by orographic lifting and mesoscale lifting from BLJ exits coupling with SLLJ entrances; and another over the Yangtze River Basin, in association with SLLJ hydraulic jumps when SLLJs pass the Nanling Mountains and the low-level convergence along shear lines. Type-O mainly enhances coastal rainfall through deep-layer convergence (shear line) from overlapping BLJs and SLLJs combined with coastal orographic lifting. Type-D produces the weakest rainfall because of relatively weak BLJs. For the same DLLJ type, events in the NSCS produce stronger rainfall than those in the BBG, and their associated rainbands are positioned further south. Moreover, as westerly disturbances move southward, SLLJs and BLJs can form different combinations over the BBG and NSCS. The concurrent presence of DLLJs in these two regions leads to a linear superposition of the precipitation patterns corresponding to the individual DLLJ types.

This study presents the first climatology of diverse DLLJ structures over the BBG and NSCS, clarifying their synoptic-scale and regional subdaily forcing processes along with their impacts on rainfall. The results extend our understanding of how LLJs at different levels modulate rainfall distribution over southern China (Du & Chen, 2019a; Li & Du, 2021), and offer new theoretical insights to enhance the forecasting of warm-season heavy rainfall. In particular, the different DLLJ structures identified in this study provide a framework for rainfall forecasting. Recognizing these structures can help predict the likely location and intensity of heavy rainfall, thereby improving precipitation forecasts and flood warnings during the Meiyu season. However, DLLJs are also common in other regions of China, such as eastern and central areas (Cui et al., 2023; Luo & Du, 2023), where they considerably influence the initiation, intensity, and duration of precipitation. Whether the DLLJ classification proposed in this study applies to other regions remains to be verified. Furthermore, this study also documents transitions between different DLLJ types, and the processes governing these transitions and their effects on rainfall evolution require further investigation. Finally, although this study compares the rainfall impacts of various DLLJ types, it is necessary to quantitatively assess the relative contributions of terrain, synoptic forcing, and DLLJ dynamics under different DLLJ types through high-resolution case simulations and sensitivity experiments.

Conflict of Interest

The authors declare no conflicts of interest relevant to this study.

Availability Statement

The Integrated Multi-satellitE Retrievals for GPM (IMERG) final run data used during this study are openly available from the Global Precipitation Mission of NASA (Huffman et al., 2023) at https://disc.gsfc.nasa.gov/datasets/GPM_3IMERGHH_07/. The fifth-generation reanalysis data set of ERA5 from the European Center for Medium-Range Weather Forecasts (Hersbach et al., 2023) is openly available at https://cds.climate.copernicus.eu/cdsapp#!/dataset/. The typhoon best-track data set (Ying et al., 2014) is available online at http://tcdata.typhoon.org.cn/. The analysis and plotting codes for this study are permanently archived on Zenodo (Zhou, 2026).

Acknowledgments
This work is supported by the National Natural Science Foundation of China (Grant: 42475003, and 42475002) and the Guangdong Project of Basic and Applied Basic Research (Grant 2020B0301030004, 2024A1515510005, and 2025A1515011974), Southern Marine Science and Engineering Guangdong Laboratory (Zhuhai) (SML2024SP035, SML2024SP012, and 311024001), Heavy Rainfall Research Foundation of China (BYKJ2024Z01), and the Key Innovation Team of the China Meteorological Administration (CMA2023ZD08). We acknowledge the high-performance computing support from School of Atmospheric Sciences of Sun Yat-sen University. We are also grateful to the three anonymous reviewers for their valuable comments.

References

Blackadar, A. K. (1957). Boundary layer wind maxima and their significance for the growth of nocturnal inversions. *Bulletin America Meteorology Social*, *38*(5), 283–290. https://doi.org/10.1175/1520-0477-38.5.283

Bonner, W. D. (1968). Climatology of the low level jet. *Monthly Weather Review*, *96*(12), 833–850. https://doi.org/10.1175/1520-0493(1968)096<0833:COTLLJ>2.0.CO;2

Chen, G. (2020). Diurnal cycle of the Asian summer monsoon: Air pump of the second kind. *Journal of Climate*, *33*(5), 1747–1775. https://doi.org/10.1175/JCLI-D-19-0210.1

Chen, G., Sha, W., Iwasaki, T., & Wen, Z. (2017). Diurnal cycle of a heavy rainfall corridor over east Asia. *Monthly Weather Review*, *145*(8), 3365–3389. https://doi.org/10.1175/MWR-D-16-0423.1

Chen, G., Yoshida, R., Sha, W., Iwasaki, T., & Qin, H. (2014). Convective instability associated with the eastward-propagating rainfall episodes over Eastern China during the warm season. *Journal of Climate*, *27*(6), 2331–2339. https://doi.org/10.1175/JCLI-D-13-00443.1

Chen, G. T., Wang, C., & Lin, L. (2006). A diagnostic Study of a retreating Mei-Yu front and the accompanying low-level jet Formation and intensification. *Monthly Weather Review*, *134*(3), 874–896. https://doi.org/10.1175/MWR3099.1

Chen, G. X., Du, Y., & Wen, Z. P. (2021). Seasonal, interannual, and interdecadal variations of the East Asian summer monsoon: A diurnal-cycle perspective. *Journal of Climate*, *34*(11), 4403–4421. https://doi.org/10.1175/JCLI-D-20-0882.1

Chen, Y., Chen, X. A., & Zhang, Y. (1994). A Diagnostic Study of the low-level jet during TAMEX IOP 5. *Monthly Weather Review*, *122*(10), 2257–2284. https://doi.org/10.1175/1520-0493(1994)122<2257:ADSOTL>2.0.CO;2

Cui, C., Zhou, W., Yang, H., Wang, X., Deng, Y., Wang, X., et al. (2023). Analysis of the characteristics of the low-level jets in the middle reaches of the Yangtze River during the Mei-yu season. *Advances in Atmospheric Sciences*, *40*(4), 711–724. https://doi.org/10.1007/s00376-022-2107-1

Cui, W., Dong, X., Xi, B., Feng, Z., & Fan, J. (2020). Can the GPM IMERG final product accurately represent MCSs' precipitation characteristics over the central and Eastern United States? *Journal of Hydrometeorology*, *21*(1), 39–57. https://doi.org/10.1175/JHM-D-19-0123.1

Dong, F., Zhi, X., Zhang, L., & Ye, C. (2021). Diurnal variations of coastal boundary layer jets over the Northern South China Sea and their impacts on diurnal cycle of rainfall over Southern China during the early-summer rainy season. *Monthly Weather Review*, *149*(10), 3341–3363. https://doi.org/10.1175/MWR-D-20-0292.1

Du, Y., & Chen, G. (2018). Heavy rainfall associated with double low-level jets over Southern China. Part I: Ensemble-based analysis. *Monthly Weather Review*, *146*(11), 3827–3844. https://doi.org/10.1175/MWR-D-18-0101.1

Du, Y., & Chen, G. (2019a). Climatology of low-level jets and their impact on rainfall over Southern China during the early-summer rainy season. *Journal of Climate*, *32*(24), 8813–8833. https://doi.org/10.1175/JCLI-D-19-0306.1

Du, Y., & Chen, G. (2019b). Heavy rainfall associated with double low-level jets over Southern China. Part II: Convection initiation. *Monthly Weather Review*, *147*(2), 543–565. https://doi.org/10.1175/MWR-D-18-0102.1

Du, Y., Chen, G., Han, B., Mai, C., Bai, L., & Li, M. (2020). Convection initiation and growth at the Coast of South China. Part I: Effect of the marine boundary layer jet. *Monthly Weather Review*, *148*(9), 3847–3869. https://doi.org/10.1175/MWR-D-20-0089.1

Du, Y., Chen, Y., & Zhang, Q. (2015). Numerical simulations of the boundary layer jet off the Southeastern Coast of China. *Monthly Weather Review*, *143*(4), 1212–1231. https://doi.org/10.1175/MWR-D-14-00348.1

Du, Y., & Rotunno, R. (2014). A simple analytical model of the nocturnal low-level jet over the Great Plains of the United States. *Journal of the Atmospheric Sciences*, *71*(10), 3674–3683. https://doi.org/10.1175/JAS-D-14-0060.1

Du, Y., Rotunno, R., & Zhang, Q. (2015a). Analysis of WRF-Simulated diurnal boundary layer winds in Eastern China using a simple 1D model. *Journal of the Atmospheric Sciences*, *72*(2), 714–727. https://doi.org/10.1175/JAS-D-14-0186.1

Du, Y., Shen, Y., & Chen, G. (2022). Influence of Coastal Marine boundary layer Jets on Rainfall in South China. *Advances in Atmospheric Sciences*, *39*(5), 782–801. https://doi.org/10.1007/s00376-021-1195-7

Du, Y., Zhang, Q., Chen, Y. Y. L., Zhao, Y., & Wang, X. (2014). Numerical simulations of spatial distributions and diurnal variations of low-level jets in China during early summer. *Journal of Climate*, *27*(15), 5747–5767. https://doi.org/10.1175/JCLI-D-13-00571.1

Du, Y., Zhang, Q. H., Ying, Y., & Yang, Y. M. (2012). Characteristics of low-level jets in Shanghai during the 2008–2009 warm seasons as inferred from wind profiler radar data. *J. Meteor. Soc. Japan*, *90*(6), 89–903. https://doi.org/10.2151/jmsj.2012-603

He, M., Liu, H., Wang, B., & Zhang, D. (2016). A modeling Study of a low-level jet along the Yun-Gui Plateau in south China. *Journal of Applied Meteorology and Climatology*, *55*(1), 41–60. https://doi.org/10.1175/JAMC-D-15-0067.1

Hersbach, H., Bell, B., Berrisford, P., Biavati, G., Horányi, A., Muñoz Sabater, J., et al. (2023). ERA5 hourly data on pressure levels from 1940 to present [Dataset]. *Copernicus Climate Change Service (C3S) Climate Data Store (CDS)*. https://doi.org/10.24381/cds.bd0915c6

Hersbach, H., & Coauthors (2020). The ERA5 global reanalysis. *Quart. J. Roy. Meteor. Soc.*, *146*, 1999–2049. https://doi.org/10.1002/qj.3803

Higgins, R. W., Yao, Y., Yarosh, E. S., Janowiak, J. E., & Mo, K. C. (1997). Influence of the Great Plains low-level jet on summertime precipitation and moisture transport over the central United States. *Journal of Climate*, *10*(3), 481–507. https://doi.org/10.1175/1520-0442(1997)010<0481:IOTGPL>2.0.CO;2

Holton, J. R. (1967). The diurnal boundary layer wind oscillation above sloping terrain. *Tellus*, *19*(2), 200–205. https://doi.org/10.3402/tellusa.v19i2.9766

Huang, W., Chan, J. C. L., & Wang, S. (2010). A planetary-scale land–sea breeze circulation in East Asia and the western North Pacific. *Quarterly Journal of the Royal Meteorological Society*, *136*(651), 1543–1553. https://doi.org/10.1002/qj.663

Huang, X., Zhang, C., Fei, J., Cheng, X., Ding, J., & Liu, H. (2022). Uplift mechanism of coastal extremely persistent heavy rainfall (EPh): The key role of low-level jets and ageostrophic winds in the boundary layer. *Geophysical Research Letters*, *49*(8), e2021GL096029. https://doi.org/10.1029/2021GL096029

Huffman, G. J., Stocker, E. F., Bolvin, D. T., Nelkin, E. J., & Tan, J. (2023). GPM IMERG Final Precipitation L3 Half Hourly 0.1 degree x 0.1 degree V07 [Dataset]. *Goddard Earth Sciences Data and Information Services Center (GES DISC)*. https://doi.org/10.5067/GPM/IMERG/3B-HH/07

Jourdier, B. (2020). Evaluation of ERA5, MERRA-2, COSMOREA6, NEWA and AROME to simulate wind power production over France. *Advances in Science and Research*, *17*, 63–77. https://doi.org/10.5194/asr-17-63-2020

Kong, H., Zhang, Q., Du, Y., & Zhang, F. (2020). Characteristics of coastal low-level jets over BBG, China, during the early warm season. *Journal of Geophysical Research: Atmospheres*, *125*(14), e2019JD031918. https://doi.org/10.1029/2019JD031918

Li, R., Wang, K., & Qi, D. (2018). Validating the integrated multisatellite retrievals for global precipitation measurement in terms of diurnal variability with hourly gauge observations collected at 50,000 stations in China. *Journal of Geophysical Research: Atmospheres*, *123*(18), 10–423. https://doi.org/10.1029/2018JD028991

Li, X., & Du, Y. (2021). Statistical relationships between two types of heavy rainfall and low-level jets in South China. *Journal of Climate*, *34*(21), 8549–8566. https://doi.org/10.1175/JCLI-D-21-0121.1

Li, Z., Chan, J. C. L., Du, Y., & Luo, Y. (2020). Statistical characteristics of pre-summer rainfall over south China and associated synoptic conditions. *Journal of the Meteorological Society of Japan*, *98*(1), 213–233. https://doi.org/10.2151/jmsj.2020-012

Lima, D. C. A., Soares, P. M. M., Semedo, A., & Cardoso, R. M. (2018). A global view of coastal low-level wind jets using an ensemble of reanalyses. *Journal of Climate*, *31*(4), 1525–1546. https://doi.org/10.1175/JCLI-D-17-0395.1

Lin, Y., & Du, Y. (2025). Sensitivity of coastal rainfall simulation to the assimilation of wind profiles near the marine boundary layer jet: An observing System simulation experiment. *Journal of Geophysical Research: Atmospheres*, *130*(15), e2025JD044106. https://doi.org/10.1029/2025JD044106

Lindzen, R. S., & Chapman, S. (1969). Atmospheric tides. *Space Science Reviews*, *10*(1), 3–188. https://doi.org/10.1007/BF00171584

Liu, X., Chen, G., Zhang, S., & Du, Y. (2023). Formation of low-level jets over Southern China in the Mei-yu season. *Advances in Atmospheric Sciences*, *40*(10), 1731–1748. https://doi.org/10.1007/s00376-023-2358-5

Liu, X., Luo, Y., Huang, L., Zhang, D. L., & Guan, Z. (2020). Roles of double low-level jets in the generation of coexisting inland and coastal heavy rainfall over south China during the presummer rainy season. *Journal of Geophysical Research: Atmospheres*, *125*(18), e2020JD032890. https://doi.org/10.1029/2020JD032890

Luo, Y., & Du, Y. (2023). The roles of low-level jets in "21·7" Henan extremely persistent heavy rainfall event. *Advances in Atmospheric Sciences*, *40*(3), 350–373. https://doi.org/10.1007/s00376-022-2026-1

Luo, Y., & Du, Y. (2025). Moisture sources and sinks of low-level jets in south China: A backward and forward trace model approach. *Journal of Climate*, *38*(11), 2641–2658. https://doi.org/10.1175/JCLI-D-24-0200.1

Ma, C., Li, Y., & Xu, B. (2023). Impact of double low-level jets on the extreme rainstorm in Henan Province in July 2021. *Chinese Journal of Atmospheric Sciences*, *47*, 1611–1625. (in Chinese with English abstract). https://doi.org/10.3878/j.issn.1006-9895.2304.22110

Monaghan, A. J., Rife, D. L., Pinto, J. O., Davis, C. A., & Hannan, J. R. (2010). Global precipitation extremes associated with diurnally varying low-level jets. *Journal of Climate*, *23*(19), 5065–5084. https://doi.org/10.1175/2010JCLI3515.1

Orlanski, I. (1975). A rational subdivision of Scale for atmospheric processes. *Bulletin America Meteorology Social*, *56*, 527–530.

Rife, D. L., Pinto, J. O., Monaghan, A. J., Davis, C. A., & Hannan, J. R. (2010). Global distribution and characteristics of diurnally varying low-level jets. *Journal of Climate*, *23*(19), 5041–5064. https://doi.org/10.1175/2010JCLI3514.1

Rotunno, R., & Bryan, G. H. (2018). Numerical simulations of two-layer flow past topography. Part I. The leeside hydraulic jump. *Journal of the Atmospheric Sciences*, *75*(4), 1231–1241. https://doi.org/10.1175/JAS-D-17-0306.1

Shapiro, A., Fedorovich, E., & Rahimi, S. (2016). A unified theory for the Great Plains nocturnal low-level jet. *Journal of the Atmospheric Sciences*, *73*(8), 3037–3057. https://doi.org/10.1175/JAS-D-15-0307.1

Stensrud, D. J. (1996). Importance of low-level jets to climate: A review. *Journal of Climate*, *9*(8), 1698–1711. https://doi.org/10.1175/1520-0442(1996)009,1698:IOLLJT.2.0.CO;2

Su, L., Hu, J., Du, Y., Li, J., & Chen, G. (2025). Boundary-Layer and low-level moisture fluxes during low-level jet events in south China and their relationship with early summer rainfall. *Journal of Climate*, *38*(7), 1691–1713. https://doi.org/10.1175/JCLI-D-23-0561.1

Wang, R., & Chen, G. (2025). A conceptual model of diurnal recharge-discharge of energy for the record-breaking heavy rains over east Asia in summer 2020. *Monthly Weather Review*, *153*(7), 1195–1217. https://doi.org/10.1175/MWR-D-24-0196.1

Wang, Z., Gao, K., & Zhai, G. Q. (2003). A mesoscale numerical simulation of low level jet realted with the southwest vortex. *Chinese Journal of Atmospheric Sciences*, *27*, 75–85. (in Chinese with English abstract). https://doi.org/10.3878/j.issn.1006-9895.2003.01.07

Xu, B. Y., & Coauthors (2023). Thermodynamics and microphysical characteristics of an extreme rainfall event under the influence of a low-level jet over the South China Coast. *Journal of Tropical Meteorology*, *29*, 216–235. https://doi.org/10.46267/j.1006-8775.2023.017

Xue, M., Luo, X., Zhu, K., Sun, Z., & Fei, J. (2018). The controlling role of boundary layer inertial oscillations in Meiyu frontal precipitation and its diurnal cycles over China. *Journal of Geophysical Research: Atmospheres*, *123*(10), 5090–5115. https://doi.org/10.1029/2018JD028368

Yang, H., Du, Y., & Sun, J. (2025). The merger of a supercell and squall line in the Great Plains. Part I: Initiation of the supercell. *Journal of Geophysical Research: Atmospheres*, *130*(13), e2024JD042393. https://doi.org/10.1029/2024JD042393

Ying, M., Zhang, W., Yu, H., Lu, X., Feng, J., Fan, Y. X., et al. (2014). An overview of the China meteorological administration tropical cyclone database [Dataset]. *Journal of Atmospheric and Oceanic Technology*, *31*(2), 287–301. https://doi.org/10.1175/JTECH-D-12-00119.1

Zeng, W., Chen, G., Bai, L., Liu, Q., & Wen, Z. (2022). Multiscale processes of heavy rainfall over east Asia in summer 2020: Diurnal cycle in response to synoptic disturbances. *Monthly Weather Review*, *150*, 1355–1376. https://doi.org/10.1175/MWR-D-21-0308.1

Zhang, M., & Meng, Z. (2019). Warm-sector heavy rainfall in southern China and its WRF simulation evaluation: A low-level-jet perspective. *Monthly Weather Review*, *147*(12), 4461–4480. https://doi.org/10.1175/MWR-D-19-0110.1

Zhang, X., Luo, Y., & Du, Y. (2024). Observation of boundary-layer jets in the Northern South China Sea by a research vessel. *Remote Sensing*, *16*(20), 3872. https://doi.org/10.3390/rs16203872

Zheng, E., Du, Y., Luo, Y., Zhang, Q., Chen, G., Su, L., & Kong, H. (2026). Two types of low-level jets in China during the warm season: Observational climatology from radiosonde data. *Atmospheric and Oceanic Science Letters*.

Zhou, C. (2026). springling/DLLJ_diversity-code: DLLJ_diversity code - Initial version (v1.1.0) [Software]. *Zenodo*. https://doi.org/10.5281/zenodo.18210977

Zhou, X., Cheng, Z., Li, H., & Hu, D. (2022). Comparison between the roles of low-level jets in two heavy rainfall events over south China. *Journal of Meteorological Research*, *36*(2), 326–341. https://doi.org/10.1007/s13351-022-1159-6